On the α-element abundance gradients in the disk of the Sculptor spiral galaxy NGC 300[1]

M. A. Urbaneja

Instituto de Astrofísica de Canarias, Vía Láctea S/N, E-38200 La Laguna, Canary Islands, Spain

maup@iac.es

A. Herrero

Instituto de Astrofísica de Canarias, Vía Láctea S/N, E-38200 La Laguna, Canary Islands, Spain.
Dpto. de Astrofísica, Universidad de La Laguna, Avda. Astrofísico Francisco Sánchez, E-38271 La Laguna, Canary Islands, Spain

ahd@iac.es

F. Bresolin

Institute for Astronomy, University of Hawaii, 2680 Woodlawn Drive, Honolulu, Hawaii 96822

bresolin@ifa.hawaii.edu

R.-P. Kudritzki

Institute for Astronomy, University of Hawaii, 2680 Woodlawn Drive, Honolulu, Hawaii 96822

kud@ifa.hawaii.edu

W. Gieren

Universidad de Concepción, Departamento de Física, Casilla 160-C, Concepción, Chile

wgieren@coma.cfm.udec.cl

J. Puls

Universitäts-Sternwarte München, Scheinerstr. 1, D-81679 Munich, Germany

uh101aw@usm.uni-muenchen.de

N. Przybilla

Dr. Remeis-Sternwarte Bamberg, Sternwartstr. 7, D-96049 Bamberg, Germany

przybilla@sternwarte.uni-erlangen.de

F. Najarro

Instituto de Estructura de la Materia, CSIC, C/Serrano, 121, E-28006 Madrid, Spain

najarro@isis.iem.csic.es

and

G. Pietrzyński

Universidad de Concepción, Departamento de Física, Casilla 160-C, Concepción, Chile
Warsaw University Astronomical Observatory, Al. Ujazdowskie 4, PL-00-478 Warsaw, Poland

pietrzyn@hubble.cfm.udec.cl

ABSTRACT

We have carried out a detailed spectral analysis of six early B-type supergiants in the Sculptor Group spiral galaxy NGC 300. To this end, we used state-of-the-art unified blanketed Non-Local Thermodynamic Equilibrium model atmospheres (computed with the code FASTWIND), aimed at the determination of the stellar parameters and of detailed surface abundance patterns. We discuss the individual evolutionary stage of each star in view of their CNO surface abundance, which we compare to massive star evolutionary models with rotation. Although the quantitative comparison does not yield a good agreement, the qualitative behaviour is consistent with the model predictions. This issue supports the idea that, although rather evolved, the stars are directly evolving from the Main Sequence and therefore they are in a pre red supergiant phase. We derive the stellar abundance gradients in the disk of NGC 300 for the elements O, Mg and Si. Using the available literature data on H II regions in NGC 300, we carry out a detailed comparison of nebular oxygen abundances resulting from different, widely used empirical calibrations. Finally, we compare the abundance gradients derived from the ISM to those derived from the blue supergiants studied in this paper. We find a O/H abundance gradient of -0.033 ± 0.026 dex arcmin^{-1} over

a distance equal to the isophotal radius of the galaxy. This trend is also followed in good agreement by Mg and Si abundances. The abundance gradients derived from our stellar data are shallower than those obtained from most previous H II region analyses, and we obtain a lower oxygen abundance in the central region of the galaxy (8.57 ± 0.13 dex), which is, however, in agreement with the H II region abundance results derived with recent calibrations of several statistical indicators.

Subject headings: galaxies: abundances — galaxies: individual (NGC 300) — galaxies: ISM — HII regions — stars: abundances — stars: atmospheres

1. Introduction

The analysis of the chemical abundance distribution in spiral galaxies is a powerful tool that allows us to constrain both their chemical evolution, as well as their star formation histories (Vila-Costas & Edmunds 1992; Garnett et al. 1997). In this respect a major rôle has been played by the study of extragalactic H II regions. From the knowledge of the electron temperature, $T_{\rm e}$, the ionic abundances of the most common elements, such as oxygen, nitrogen and sulphur, can be directly derived from the spectra of ionized nebulae, and transformed into absolute abundances accounting for the unseen ionization stages, by means of ionization correction factors (Osterbrock 1989; Pagel 1997). However, often the temperature-sensitive diagnostic lines (e.g. the auroral [O III] λ4363, [N II] λ5755 and [S III] λ6312) are too weak to be detected, and therefore a direct determination of chemical abundances is no longer possible. This is the situation for metal-rich H II regions located near the nucleus of their parent galaxy, and for abundance studies of galaxies at high redshift (Lilly, Carollo & Stockton 2003; Steidel et al. 2004; Pettini & Pagel 2004).

In those cases where the auroral lines cannot be measured, abundance determinations rely on statistical empirical methods, the so-called strong-lines methods (Stasińska 2004; Garnett 2004). In short, ratios of the strongest observed emission lines are used to have a rough idea of oxygen abundances. The most commonly applied ratio, the R_{23} index, is based on the total [O II] λ3727 + [O III] $\lambda\lambda$4959,5007 oxygen line intensity relative to Hβ (Pagel et al. 1979). Since the introduction of this indicator, several authors have presented calibrations of the R_{23} vs O/H relationship. Among others, we cite here the works of Edmunds & Pagel (1984), Dopita & Evans (1986), Skillman (1989), McGaugh (1991), Zaritsky,

[1]Based on observations obtained at the ESO Very Large Telescope

Kennicutt & Huchra (1994), and Pilyugin (2000, 2001). Strictly speaking, the calibration of this indicator in terms of the oxygen abundance needs a large set of independent, well-determined abundances from a direct method. However, the key $T_{\rm e}$-diagnostic lines have been commonly observed only for metallicities approximately below $0.5Z_{\odot}$. Only recently faint auroral lines, in particular [N II] λ5755 and [S III] λ6312, have been detected at O/H abundances even higher than solar (Bresolin, Garnett & Kennicutt 2004a; Garnett, Kennicutt & Bresolin 2004; Castellanos, Díaz & Terlevich 2002). Therefore, at higher metallicities the available R_{23} calibrations rely on photoionization models alone (Kobulnicky, Kennicutt & Pizagno 1999; Charlot & Longhetti 2001; Kewley & Dopita 2002).

One of the major drawbacks of the R_{23} index is that it shows a double-valued behaviour with oxygen abundance. Besides, it has been shown that the R_{23} indicator depends not only on the oxygen abundance but also on the hardness of the ionizing radiation and on the geometrical characteristics of the nebulae, which is usually described by means of the *ionization parameter* (Osterbrock 1989). Some of the widely used R_{23} calibrations consider the latter dependence (e.g. Kobulnicky et al. 1999), while others neglect it (e.g. Zaritsky et al. 1994). Additional factors, including the incompleteness of the calibration datasets and physical effects not yet considered in photoionization models (Pilyugin 2003; Garnett 2004) contribute to make the derived H II region oxygen abundances to depend strongly upon the choice of calibration (Kewley & Dopita 2002; Cedrés 2003).

Other indicators of the oxygen abundance have been introduced, to circumvent some of the difficulties affecting the calibration of R_{23}. For example, the S_{23} index proposed by Díaz & Pérez-Montero (2000), which varies monotonically over the range in which R_{23} becomes double-valued, and the [N II]/Hα indicator (Denicoló, Terlevich & Terlevich 2002; Pettini & Pagel 2004), which is well correlated with the oxygen abundance over the range for which it is calibrated, although it is affected by a large dispersion in the results.

In their work on M101, Kennicutt, Bresolin & Garnett (2003) have found systematic abundance differences, up to 0.5 dex, between oxygen abundances derived by means of commonly used statistical indicators and the ones obtained from direct measurements of $T_{\rm e}$, with the latter being lower. In the case of M101 this implies a difference in the central oxygen abundance of about a factor of two between the two methods. Similar discrepancies have been found in M51 by Bresolin, Garnett & Kennicutt (2004a). As a consequence, oxygen abundances derived in the low-excitation H II regions of spiral galaxies over the last two decades are likely to be overestimated by factors of 2-3.

It is clear that, along with new comparisons between the direct and the statistical meth-

ods, an independent way to determine the oxygen abundances in galaxies is highly desiderable. The early work by Unsöld (1955) showed that the analysis of hot star atmospheres can provide us with a complementary approach to the problem of abundance determination. The first work on the Galactic abundance gradient from spectra of B-type stars dates back to Gehren et al. (1985). In recent years, the work by Smartt & Rolleston (1997, see Herrero 2003 for a review) has shown the importance of such stellar work in our Galaxy. The generation of 10m-class telescopes opens the window to a more distant Universe. The first reference to their potential impact on extragalactic stellar spectroscopy is due to Kudritzki et al. (1995). Following this seminal work, several authors have carried out the analysis of chemical abundances of hot stars in galaxies of the Local Group, including M31 (McCarthy et al. 1995; Venn et al. 2000; Smartt et al. 2001; Trundle et al. 2002) and M33 (McCarthy et al. 1997; Monteverde et al. 1997; Monteverde, Herrero & Lennon 2000). More recently, a few supergiants in nearby dwarf galaxies have been added to this list (Venn et al. 2003; Kaufer et al. 2004). Quantitative stellar spectroscopy has also been extended to galaxies beyond the Local Group, out to ~ 7 Mpc (Bresolin et al. 2001), including the detailed analysis of an emission line star (Bresolin et al. 2002b) and two early B-type supergiants (Urbaneja et al. 2003, hereafter Paper I) in NGC 300 at 2 Mpc .

The analysis of single stars in external galaxies does not only provide us with chemical abundance patterns, which are required for studies of galactic evolution and nucleosynthesis. It also provides constraints for the theory of stellar structure and evolution at different metallicities and environmental conditions, allowing us to test the recent models incorporating the effects of rotational mixing, that may also depend on the metallicity (Maeder & Meynet 2000; Heger & Langer 2000). Moreover, massive blue supergiants may in the future be used as standard candles by means of the Wind Momentum – Luminosity Relationship (Kudritzki & Puls 2000, and references therein) or the Flux-Weighted Gravity – Luminosity Relationship (Kudritzki, Bresolin & Przybilla 2003). In this context, it is important to determine mass loss rates and stellar parameters for supergiant stars at different metallicities. External galaxies with strong metallicity gradients are natural targets for such endeavours.

In Paper I we have shown how the combination of low-resolution spectroscopy and state-of-the art model atmospheres of hot luminous stars can yield detailed information about the chemical composition of early B-type supergiants in galaxies beyond the Local Group. In particular, we have been able to derive, for two stars in the Sculptor Group late-type spiral galaxy NGC 300, a detailed abundance pattern including the key elements C, N and O, as well as Mg and Si.

This paper presents the analysis of four additional B-type supergiant in NGC 300, dis-

tributed across the disk of the galaxy, that complements the previous analysis, allowing us to compare the oxygen abundance trend obtained through the application of several strong-lines abundance indicators to H II region data taken from the literature. The analysis of the B-type supergiants yields also for the first time the spatial trends of two other α-elements, Mg and Si. We point out that NGC 300 is a key galaxy in the Araucaria Project (Gieren et al. 2001) which seeks to provide improved calibrations of the environmental dependences of a number of stellar distance indicators, including blue supergiants and Cepheids. The determination of the abundance gradients in the disk of NGC 300 is a fundamental step for the calibration of the effect of metallicity on Cepheid luminosities, a study we are planning for the near future taking advantage of the recent discovery of more than 100 Cepheid variables in this galaxy (Pietrzyński et al. 2002).

2. Observations

As in Paper I, we used the observational dataset described in Bresolin et al. (2002a, blue spectra) and Bresolin et al. (2002b, Hα spectra), obtained in two separate runs at the ESO Very Large Telescope with FORS (Focal Reducer and low-dispersion Spectrograph). The observed spectra cover almost completely the 3800 - 7200 Å wavelength range at R$\sim$1000 resolution. The reader is referred to Bresolin et al. (2002a) and to Bresolin et al. (2002b) for a complete description of the observations, as well as for the designation used here for the blue supergiants.

After a careful inspection of the whole sample, we selected those early B-type supergiants that showed high S/N and no evidence for serious contamination by H II regions, or any indication of being unresolved small clusters of stars. Although B-12 and B-15 showed some nebular contamination, we included them because B-12 is the star closest to the galactic center among those observed, while B-15 samples the intermediate regions of the galaxy, and hence they are very important for the comparison with ISM abundances.

3. Spectral analysis

The model atmosphere code (FASTWIND, Santolaya-Rey, Puls & Herrero 1997; Puls et al. 2003) as well as the analysis technique applied were described in Paper I and we will not repeat the details here. As a guideline, we schematically list below the main features of the analysis:

- the effective temperature and an estimation of the microturbulent velocity are obtained

using the Si lines. The Si ionization balance (Si II/Si III or Si III/Si IV, depending on the lines present in the spectrum) is used as the Teff indicator. The lines of the strong Si III triplet 4552/4567/4574 are used to infer the microturbulent velocity (see below)

- the surface gravity and the mass-loss rate are determined from H Balmer lines
- oxygen abundance: the O II line blends at $\lambda\lambda$4070-80, $\lambda\lambda$4317-19 and $\lambda\lambda$4414-16 are used
- nitrogen abundance: the N II λ3995 line and the blend with He I at $\sim$ 5050,5100 Å are considered
- carbon abundance: we use the C II line λ4267 as the main indicator for carbon abundances. The blend of C II lines at $\lambda\lambda$6578-80 is also used when observed, although giving always more weight to the λ4267 Å line
- magnesium abundance: it is derived from the Mg II line at λ4481

We note that because of the low resolution, we do not try to fit any particular metal feature, but instead we try to reproduce the whole observed spectrum, i.e. we consider as "best solutions" those models which best reproduce the global features in the observed spectra. The presence of a large number of weak metal lines in the 4600 - 4700 Å wavelength range makes the selection of the continuum level in this area difficult. Good S/N ratio (above 50) is also needed to discriminate between real features and noise.

Although a detailed analysis of the microturbulent velocity cannot be performed for each element, the relative strengths of the three components of the Si III triplet at $\sim 4550-4580$ Å can be used to infer an appropriate value for this parameter. The analysis can be started adopting an initial value common to all spectral types, say 15 km s^{-1}, typical of Galactic B supergiants (McErlean, Lennon & Dufton 1999; Smartt et al. 2001). The adopted initial value will be modified later during the detailed analysis. The assumption of a single initial turbulent velocity for all spectral types can be relaxed by adopting a lower value for later types and a larger one for earlier types (10 km s^{-1} for mid-B, and 20 km s^{-1} for O9/B0 stars).

Oxygen and nitrogen abundances can be very well constrained because of the presence of many features from these species: lines of singly ionized ions from both atoms in fact dominate the observed spectral range. On the other hand, only one line is available for both magnesium and carbon, which makes their abundances not as well constrained as for the other atoms.

3.1. Individual comments

Although stars A-9 and B-12 were presented in Paper I, we include these stars here for completeness. We retain the original classifications by Bresolin et al. (2002a) for all of the stars.

A-9 looks like a normal B1 star, with lower metallicity than the Galactic comparison stars, but larger than the SMC ones. It shows a partially re-filled Hα profile, which points to a mid-strength mass outflow.

B-12 only the higher Balmer lines have been considered for the surface gravity determination, since the cores of Hγ and Hβ are particularly affected by the nebular line subtraction. The strength of the metal features indicates an early type and high metallicity. The Hα profile, although affected by nebular contamination, is clearly in emission due to a strong mass-loss rate.

B-13 is the visually brightest object analysed, which translates in one of the best quality spectra. The star closely resembles the Galactic B3-type supergiants used as a reference. We derive a mid metallicity and the mass-loss rate is moderately strong. During the analysis, two main problems were found; firstly, the observed higher lines of the H Balmer series are stronger than in the models (this also happens with respect to the Galactic comparisons); and secondly, an unrealistic magnesium abundance is required to fit the Mg II line. This could be reflecting the presence of other(s) star(s), affecting also the observed magnitude. In fact, ACS/HST images (HST GO proposal 9492, PI: Bresolin) show a much fainter companion star $\sim$0.35 arcsec to the SE, but contributing at the level of 0.1 mag to the observed magnitude. There are no other signs in the spectrum of this object being an unresolved star cluster, and from the other elements we do not find any other warning. However, the Mg II line profile is heavily distorted, despite the general high quality of this spectrum. In the following, we will not use the derived magnesium abundance of this star

B-15 the lack of strong Si IV and Si II lines points to a mid-type star, B1.5 - B2, as classified by Bresolin et al. (2002a). Like the other stars analysed in the central field of the galaxy, this star shows in its spectrum contamination from a H II region, with the stellar Hα and Hβ lines lost in the nebular emission, and Hγ is affected, too. Fortunately, Hδ seems to be less contaminated. There are no other H Balmer lines observed for this star. A good global match of the observed spectrum can be achieved, although we cannot measure the

mass-loss rate. In particular, we cannot get any information about the β-exponent of the wind velocity law (see Paper I) and hence we adopt the same value found for the other mid B-type supergiants, $\beta = 2$. The derived mass-loss rate shall be considered an upper limit, due to the problems cited above. The stellar metallicity is slightly below solar.

C-14 shows the spectrum of an early B supergiant with intermediate metallicity. It has been classified as B1 by Bresolin et al. (2002a). The determination of the nitrogen abundance for this star is not an easy task because the nitrogen lines are weak and the N II λ3995 Å is in a region particularly distorted by the noise. This is also true for the Mg II line, which almost disappears in the noise. It has a low mass-loss rate.

D-8 the presence of the Si II λ4128-30 blend, along with the strength of the Si III triplet, the metal features between 4600 and 4700 Å and the strong Mg II line point to a mid type with intermediate metallicity, in accord with its classification as B1.5 by Bresolin et al. (2002a). The Hα profile is affected by the nebular line subtraction, but from other Balmer lines we expect a low density mass outflow.

3.2. Results

We summarize in Table 1 the stellar parameters deduced from the best-fitting models, while Table 2 shows the comparison between the observed and the synthetic magnitudes, needed to derive the stellar radius. For the observed magnitudes, we consider the new values determined after the introduction of improved zero-point calibrations (Bresolin et al. 2004b). Due to that both A-9 and B-12 present more reddening (and extinction), resulting in somewhat larger luminosities when compared to the Paper I.

Uncertainties on the effective temperatures and the surface gravities (as well as on the β parameters and the mass-loss rates) are obtained from model comparisons. Fig. 1 shows the observed Hδ and Hγ profiles of C-14 (the star with the lowest S/N in our sample) and three synthetic models for different surface gravities: the solid line corresponds to the final derived surface gravity while the two others correspond to $+0.15$ dex and -0.15 dex (dotted and dashed lines respectively) with respect to the previous one. The uncertainties found for this star are also considered for the other stars in the sample. We prefer this conservative approach rather than a detailed individualized uncertainty analysis due to the low spectral resolution. Once again, it has to be noted that these uncertainties on the effective temperatures and the surface gravities are based on the fits to the lowest S/N

spectrum present in the sample.

As an example of the quality that is commonly achieved we display in Fig. 2 four strategic wavelength regions of the observed spectrum of C-14 and its final fit, together with two additional models in order to define the abundance uncertainty. The uncertainty is estimated to be $\pm$ 0.2 *dex* from model comparisons, except for C-14, for which we have increased the uncertainty to $\pm$ 0.3 *dex* to account for the lower S/N ratio of its spectrum. Tab. 3 and Tab. 4 present a detailed investigation of the metal abundance uncertainties due to each fundamental stellar parameter (surface gravity, effective temperature, microturbulence, helium abundance, background metallicity and the wind strength) for two models representative of our sample of NGC 300 B-type supergiants. An estimation of the global abundance uncertainty for each element is also provided in these tables, showing a good agreement with our initial estimation based on model comparisons.

We adopt the Grevesse & Sauval (1998) results as the solar abundance reference, except for oxygen, for which we use the determination of Allende Prieto, Lambert & Asplund (2001, 8.69 ± 0.05 dex). Note that this introduces a small shift in the relative results (i.e. in the mean metallicity compared to the Sun) of *B-12* and *A-9* with respect to Paper I, in which we used the oxygen abundance value from Grevesse & Sauval.

We define the characteristic metallicity as the sum of the α-elements abundances, $X_{Si} + X_{Mg} + X_O$, and refer it to the solar metallicity, obtained in the same way (the entry labeled as Z in Table 1). The stars sample a wide metallicity range, from almost solar for *B-12* to $0.4 - 0.3\ Z_\odot$ for *A-9*, the B Sg star at the largest distance from the center of NGC 300 considered in this work. Silicon and magnesium abundances follow the behaviour of the O abundances.

3.2.1. Evolutionary status

Fig. 3 shows the position of the stars in the H-R diagram, where the tracks from Meynet & Maeder (2003) for solar metallicity and from Meynet & Maeder (2004) for 1/5 solar metallicity are overplotted. It is evident that according to their position in the diagram all stars are post-Main Sequence objects. This is not surprising, as we have a strong observational bias towards the brightest objects, which is reflected in large stellar radii and thus in evolved objects. At the same time, we selected apparently "normal" B-type supergiants, since none of the stars lies beyond the Humphreys-Davidson limit. Our stars are highly evolved B-supergiants, either in their way to the red supergiant (RSG) phase or in their way back to the blue (note that different stars may be in different situations).

The comparison of evolutionary and spectroscopic masses give us further information. Although recent analyses indicate that the infamous mass discrepancy between these masses is now close to a solution (Herrero, Puls & Najarro 2002; Repolust, Puls & Herrero 2004) problems still persist and are largest in the mass range of our stars. Five out of seven stars with spectroscopic masses lower than 25 $M_{\odot}$ considered by Repolust et al. (2004) show an important difference between the evolutionary and the smaller spectroscopic masses (although errors in both quantities are large). Our results are consistent with those findings: our spectroscopic masses are sistematically lower than those derived from the evolutionary tracks, although error bars are large and sometimes overlap. Even so, the differences in masses are too small to be interpreted as due to the stars evolving through long blue loops.

In Fig. 4 we have plotted the (N/O) vs (N/C) behaviour of our stars, comparing with the evolutionary models with mass loss and rotational mixing previously cited. The models shown have initial rotational velocities of 300 $\mathrm{km\,s^{-1}}$, and metallicities of Z=0.02 and Z=0.004. The high metallicity models have a ZAMS mass of 40, 25 and 20 $M_{\odot}$, while the low metallicity one is for the 30 $M_{\odot}$ model. The behaviour at each metallicity is only weakly dependent on the mass of the model. We have somewhat arbitrarily divided the stars in low metallicity ($Z < 0.51\ Z_{\odot}$) and high metallicity ($Z > 0.51\ Z_{\odot}$) bins. We see that the qualitative behaviour is consistent with the model predictions. Given the large uncertainties (initial ZAMS and rotational velocity, large errors in abundance ratios) we think that the agreement between theoretical predictions and observed values is satisfactory, especially when we consider the possibility of smaller mixing for the lower metallicity stars. This can either be due to different initial rotational velocities or to mixing efficiencies different from the model predictions. In fact, we can even trace a sequence of evolutionary status going from B-12, the less evolved star, to D-8, the most evolved object in terms of the N/C ratio. Note, however, that there are other possible criteria. For example, star B-13 is the only one with high helium abundance, and therefore it would be the most evolved object from that point of view. We also note here that the relation between helium abundances and N/C ratios is qualitatively consistent with the model predictions.

Taking advantage of the good correlation between N/C and N/O, we use one of them (N/C) as an indicator of the stellar evolutionary status, and plot it in Fig. 5 versus the effective temperature. Looking at those stars with the higher metallicity we can see that their behaviour can be explained if star B-12 (the one with the lower N/C ratio) had a low initial rotational velocity, and the mixing efficiencies for the other two stars are lower than indicated by the models (again, because of lower initial rotational velocities or due to model deficiencies). Comparison at the lower metallicity end indicates however larger efficiencies for A-9 and D-8.

In spite of these difficulties, the agreement can be considered good and the obtained abundances are indicative of pre-RSG phases. In the figure we can see that the RSG phase generates a boost in the N/C ratio at the stellar surface. Thus we conclude that the data strongly support the idea that we are looking at rather evolved supergiants, but still in the redward phase. This is in agreement with the recent results by Przybilla (2002) for a sample of A-type supergiants in different galaxies of the Local Group. During these evolved stages of massive stellar evolution the oxygen surface abundance is usually assumed to be not affected by the CNO cycle. However, evolutionary models with rotational mixing predict significant variations at earlier stages of evolution. To clarify this point we have used the derived Si/O ratio, since from our current understanding of stellar evolution we do not expect any contamination of the Si abundance until very late in the course of the stellar evolution (Woosley, Heger & Weaver 2002). In Fig. 6 we show the [Si/O] ratio vs the stellar metallicity. It suggests a good correlation between O with Si, implying that the measured oxygen abundance is representative of the original one.

3.2.2. Stellar wind properties

Derived stellar wind parameters are reported in Tab. 1. As in Paper I, we adopted the wind terminal velocities according to the spectral types of the stars, for which we consider the calibration given by Kudritzki & Puls (2000, see their Tab. 1). Recent UV studies of B-type supergiants in different metallicity environments (Bresolin et al. 2002c; Urbaneja et al. 2002; Evans et al. 2004) support the idea of a weak metallicity dependence. Also from the theoretical point of view, a large effect is only expected at very low metallicities or very low wind densities (Puls et al. 2000; Vink et al. 2000; Kudritzki 2002), which is not the case for supergiant stars. It is important to note that the adopted wind velocities have an effect on the derived mass-loss rates: the higher the v_∞ is, the larger the mass-loss rate needed to fit the same Hα profile. But, because of the marginal metallicity dependence of v_∞, we do not expect to introduce a large effect on derived $\dot{M}$.

The values we obtain for the exponent of the wind velocity law, β, are consistent with the values derived from the analysis of Hα profiles of Galactic B-type supergiants (Kudritzki et al. 1999). The quoted errors are derived from model comparisons.

Concerning the mass-loss rates, it is more interesting to perform a discussion in terms of the Wind Momentum – Luminosity Relationshop, WLR. The theory of radiation driven winds (Kudritzki & Puls 2000, and references therein) predicts a tight relationship between the mechanical momentum carried by the stellar wind and the luminosity of the star

$$\dot{M}\, v_\infty\, R_*^{1/2} \propto L^x$$

being $\dot{M}$ the mass-loss rate, v_∞ the wind terminal velocity, R_* the stellar radius and L the stellar luminosity. This relationship, once properly understood and calibrated, could have many applications: as a spectroscopic distance indicator, as a recipe for stellar evolutionary models or to estimate the energy deposition from OB associations in the interstellar medium. In the case of B-type supergiants, from an analysis of a Galactic sample, Kudritzki et al. (1999) concluded that the stars show in fact two different relationship, one for the early types (B0 - B1) and another one for mid types (B1.5 and later types). This result represents a challange to the theory of radiation driven winds, which cannot explain the low values of the mass-loss rates derived for mid B-types.

From the theoretical side it is also expected a metallicity dependence of $\dot{M}$, larger than the one for v_∞. Recent theoretical calculations predicts a power-law dependence with a total exponent of the order of 0.64 (Vink et al. 2001). These authors conclude that the modified wind momentum rate, $D_{mod} = \dot{M}\, v_\infty\, R_*^{1/2}$, should obey a metallicity dependent power-law with an exponent of ~ 0.8 .

Because of the range of metallicities in our sample, it is interesting to perform an exploratory analysis of the derived WLR. Before that, it is important to note that while the metallicity we derive for each star in based on α-element abundances, what really determines the mass-loss rate is the radiative acceleration in the transonic wind regime, which in the metallicity range and effective temperature range of our sample, is driven by the iron group elements (Puls et al. 2000; Vink et al. 2000, 2001). Therefore, because of the low number of stars in our sample and without the knowledge of iron group elements abundances, we will not try a detailed comparison with the theoretical predictions.

Fig. 7 shows the WLR of the NGC 300 B-type supergiants compared to previous studies in the Galaxy. Solid lines, both thin and thick, are the Galactic WLR fits determined by Kudritzki et al. (1999) for early and mid B-type supergiants respectively. We must note that these authors used unblanketed models in their study. Recent works by Herrero et al. (2002) and Repolust et al. (2004) have shown that the analysis of Galactic O-type stars by means of blanketed models requires larger mass-loss rates than previous unblanketed analyses. We can expect a similar effect for B-type supergiants. In order to clarify that issue, we have included in the figure the results for five Galactic B-type supergiants taken from Urbaneja (2004). The dashed line represents the original Kudritzki et al. (1999) fit for early B-types shifted by 0.25 dex. Although we must be very careful due to the low number statistics, this displacement perfectly matches the new results for the three early B Galactic stars (the solid circles in the figure). The results for NGC 300 early B-type supergiants (represented by stars in the figure) are consistent with the new position for Galactic stars in view of their (α-elements) metallicities: B-12 ($Z_\odot$) follows the trend given by the three Galactic stars,

while C-14 and A-9 (both $\sim 0.4\,Z_{\odot}$) are located below.

On the other hand, the situation is puzzling for the mid B-type stars (represented by diamonds in Fig. 7). In principle, we would expect a similar behaviour when comparing the location of B-13 (near solar metallicity) and D-8 ($\sim 0.5\,Z_{\odot}$) with the two Galactic mid B-type supergiants from Urbaneja (2004, denoted by squares). While B-13 together with the two Galactic stars seems to form a good relationship, D-8 although at lower α-element abundances fits into the same trend. One possible interpretation for that is the star being actually an unresolved group of stars (D-8 is the only one star in the sample not included in the ACS/HST GO proposal 9492), although the analysis of its blue spectrum shows no warnings about being polluted by the presence of other stars. Another possibility is that this star is located at the high $\dot{M}$-side of the so-called bi-stability jump (Lamers et al. 1995). From observations of Galactic stars, Lamers et al. (1995) located this jump at Teff ~ 21000 K, which is hotter that the one we derive for D-8. Note, however, that Lamers et al. (1995) obtained this Teff based on previous analyses which did not consider the blanketing/blocking effects on the effective temperature scale of supergiant stars (Herrero et al. 2002; Repolust et al. 2004). New analysis be means of blanketed models will probably locate the jump closer to the Teff derived for D-8. Lastly, the iron group abundances for this particular star could be closer to the values for B-13 and the Galactic stars, and then D-8 must follow the same trend. Without any ad hoc assumption, we have no final explanation for this result at this point.

4. Radial abundance gradients of the α-elements in NGC 300

4.1. Oxygen abundance gradient

4.1.1. H II regions: comparison between strong line methods

The most comprehensive study of the oxygen abundance in the ISM of NGC 300 has been carried out by Deharveng et al. (1988). These authors used their own data as well as observations from previous studies (Pagel et al. 1979; Webster & Smith 1983; D'odorico et al. 1983; Edmunds & Pagel 1984) to infer the oxygen abundance gradient in this galaxy. There is a more recent work on the S/H and O/H abundances in the ISM of NGC 300 by Christensen, Petersen & Gammelgaard (1997), but the spatial coverage of their H II region sample is reduced with respect to the Deharveng et al. (1988) dataset.

Before comparing the stellar and nebular abundances for NGC 300, we need to discuss

the dependence of the latter on the empirical abundance calibration. To this end, we apply different R_{23} calibrations to the observational dataset of Deharveng et al. (1988). Fig. 8 displays the comparison between the results of several strong line methods; each axis is labeled with an identifier of the calibration: ZKH94 stands for Zaritsky et al. (1994), KKP99 identifies the calibration by Kobulnicky et al. (1999), P01 is used for Pilyugin (2001) and KD02 denotes the *optimum abundance indicator* proposed by Kewley & Dopita (2002). These four calibrations were selected because they are among the most often used in extragalactic H II region studies. We want to stress that all the calibrations have been applied to the same observational dataset. A total number of 25 H II regions from the original dataset are considered under the first three calibrations, while only those with [N II] meassurements can be considered for the KD02 indicator (a total of 13 regions). We do not include the error bars for the sake of clarity.

The comparison between the ZKH94 and KKP99 calibrations (Fig. 8, bottom row, first column) shows a good correlation above 8.5 dex, displaying a shift from the 1:1 relation, with slightly increasing differences for increasing oxygen abundances. In this region, the abundances obtained with ZKH94 are larger. Below $\sim$ 8.5 dex, the relation shows a different slope, which can be understood as the result of the fact that while the calibration by Kobulnicky et al. considers the effects of the ionization parameter, Zaritsky et al. only considered the effect of the oxygen abundance in their calibration. Below this knee, the abundances from KKP99 seem to be larger, although this is uncertain due to the small number of H II regions in this abundance range.

In the case of the ZKH94-P01 comparison (top row, first column in Fig. 8) there is some degree of correlation, but far from the 1:1 relation and with a large scatter. Again, the relation seems to change slope around 8.5 dex, but in this case it is less evident than in the previous comparison. The oxygen abundances derived with the ZKH94 calibration always yields larger values, up to 0.5 dex, than the calibration by Pilyugin.

The comparison between the *optimum indicator* by Kewley & Dopita and the R_{23} calibration by Zaritsky et al. (Fig. 8, middle row, first column) displays a good agreement, with a small shift toward larger abundances by the latter. We must note, however, that this is a sort of fictitious concordance, since the Kewley & Dopita abundance indicator is actually the mean of the ZKH94 and KKP99 calibrations for abundances below 8.9 dex (almost all the H II regions considered in the plots). This is also true, of course, in the comparison between the KKP99 and KD02 R_{23} - O/H calibrations (middle row, second column, in the same figure).

The calibration by Pilyugin shows a good correlation with the one by Kobulnicky et al., with a scatter that increases towards the lower abundances but again far from the 1:1

relation. The slope of the relation is almost constant, even below the knee of the R_{23} - O/H relationship around 8.5 dex, which probably reflects the fact that both calibrations, although in different ways, consider the effect of a second parameter that characterises the hardness of the ionizing radiation. However, there is a large shift (0.2 - 0.3 dex), with the KKP99 calibration always yielding larger oxygen abundances.

The comparison of the P01 abundances with the KD02 ones (Fig. 8, botton row, second column) is probably of the same quality as in the case of P01-ZKH94 comparison, which again reflects the fact that the *optimum indicator* is a mean of the Kobulnicky et al. and Zaritsky et al. calibrations for abundances below 8.9 dex.

We must clarify an important point. In the application of the R_{23} - O/H calibrations by Kobulnicky et al. (1999) and Pilyugin (2001) we considered that all the H II regions belong to the "upper metallicity branch" (see below). As discussed by Kennicutt et al. (2003) this procedure is somewhat risky because we cannot be sure that any H II region belongs, a priori, to this branch, even if we derive an oxygen abundance which is in agreement with this assumption. Moreover, Bresolin, Garnett & Kennicutt (2004a) have shown severe pitfalls in the use of the Pilyugin (2001) calibration, and in general of all semi-empirical calibrations available today at high metallicity.

These comparisons allow us to illustrate how the application of several widely used R_{23} - O/H calibrations produce completely different results, even when they are applied to the same observational dataset. There is a factor of 3 difference, for example, between ZKH94 and P01 abundances for the high metallicity regions. This makes it also clear that we need an independent method for extragalactic abundance determinations.

4.1.2. Comparison between H II regions and the early B-type supergiants

We can proceed now with the comparison between stellar and nebular oxygen abundance gradients. In order to obtain the spatial location of the stars, we have used the geometrical parameters of NGC 300 given in Table 1 of Deharveng et al. (1988), after correcting all those quantities that are affected by the distance, for which we have used the value from Freedman et al. (2001, $\mu = 26.53$ mag which corresponds to 2.02 Mpc). The radial coordinate will be expressed in terms of the fractional isophotal radius ($\rho_0 = 9.75$ arcmin, or 5.73 kpc adopting the distance given above).

Fig. 9 shows the comparison between H II abundances (filled dots) and the results of our analysis of B-type supergiants (five-peaks stars), for the different calibrations of R_{23}

discussed above. Errors in the determination of the H II oxygen abundances are computed from the observational uncertainties quoted by Deharveng et al. (1988), excluding from the weighted least-squares fits those regions without observational uncertainties. We have also included in the plots the two H II regions with a direct measurement of T_e (and therefore a direct determination of its O/H, denoted by the four-peaks empty stars): Webster 7 (from Webster & Smith 1983), located at 0.39 ρ_0 from the galaxy center, has an abundance 12+log(O/H)=8.60, while Pagel 7 (from Pagel et al. 1979), which is located at 1.05 ρ_0 from the galaxy center, has an abundance 12+log(O/H)=8.23.

We can directly transform the B supergiant oxygen abundance radial distribution into a gradient. As discussed in a previous section, these stars only show CNO-cycle contamination in their C and N abundances, while there is no evidence of contamination in their O abundances, as indicated by the ratio of O to Si or Mg abundances. By assuming therefore that they show the original O abundances, we obtain a stellar gradient:

$$log(O/H) + 12 = (8.58 \pm 0.13) - (0.32 \pm 0.26)\, \rho/\rho_0$$

equivalent to $-0.05\,(\pm 0.04)$ dex kpc^{-1} .

The original gradient obtained by Deharveng et al. (1988) is based on the R_{23} calibration by Dopita & Evans (1986), which yields an oxygen ISM gradient of

$$\log(O/H) + 12 = (8.95 \pm 0.04) - (0.63 \pm 0.10)\, \rho/\rho_0$$

corresponding to $-0.11\,(\pm 0.02)$ dex kpc^{-1} .

The top panel of Fig. 9 displays the results of the R_{23} calibration by Zaritsky et al. (1994), that applies only to the upper branch.

This calibration yields an oxygen gradient of

$$\log(O/H) + 12 = (8.98 \pm 0.04) - (0.54 \pm 0.09)\, \rho/\rho_0$$

equivalent to $-0.09\,(\pm 0.02)$ dex kpc^{-1} and which is in good concordance with the Deharveng et al. (1988) results, both in slope and central abundance. It can be seen that only two of the B -type supergiants, *C-14* and *A-9* (the stars located at 0.66 ρ_0 and 0.97 ρ_0, respectively), are compatible, within the errors, with this calibration. Although the slope is compatible with ours, the galactic central oxygen abundance is not, being for the Zaritsky et al. calibration

well above the solar value while in the case of B-type supergiants it is just below the solar value.

The analytical fits to the photoionization models by McGaugh (1991) given by Kobulnicky et al. (1999) provide us with another calibration for the upper branch of the R_{23} - O/H relation, for which we obtain (see the second panel of Fig. 9)

$$\log(O/H) + 12 = (8.75 \pm 0.04) - (0.27 \pm 0.09)\, \rho/\rho_0$$

corresponding to $-0.047\,(\pm 0.016)$ dex kpc^{-1} (panel labeled as *KKP99* in Fig. 9). In contrast to the previous calibration, this produces a central oxygen abundance and slope which are compatible with the stellar results.

Recently, Pilyugin (2000; 2001) has produced new calibrations for the R_{23} - O/H relationship, based on a P-parameter that in some way takes into account the hardness of the ionizing radiation. We have applied the upper branch of Pilyugin's calibration, excluding from the calculation of the oxygen gradient those H II regions which yield abundances lower than 8.25 dex, that is the limit quoted by Pilyugin (2001) for the calibration; these regions have been marked with an empty dot in the corresponding panel of Fig. 9. Once more, we want to estress that this is not completely justified (see discussion in Kennicutt et al. 2003). The agreement between H II regions and stellar abundances is the best one. For this calibration we obtain

$$\log(O/H) + 12 = (8.52 \pm 0.06) - (0.28 \pm 0.12)\, \rho/\rho_0$$

with an effective slope of $-0.05\,(\pm 0.02)$ dex kpc^{-1} .

The stellar abundances also fit the nebular results obtained when using the calibration by Kobulnicky et al. (1999), but shifted by about *+0.2 dex*. The slopes of the nebular abundance gradients obtained with the Pilyugin and Kobulnicky et al. calibrations agree very well.

We performed a further exploration of the comparison between the stellar O/H abundances and the ISM ones obtained by means of the recent calibration of the N2 indicator (Storchi-Bergmann, Calzetti & Kinney 1994) by Pettini & Pagel (2004). This O/H abundance indicator is based on the [N II] λ6584/Hα line ratio. As mentioned before, this index shows a good correlation with the O/H abundances, but it is affected by a large scatter (which in part can be explained as produced by the inclusion in the calibration of regions with different N/O abundance ratios).

Using the Deharveng et al. line fluxes, assuming Hα/Hβ = 2.86 and [N II] λ6584 / [N II] λ6548=3, we obtain the O/H abundance gradient displayed in Fig. 10. As in previous figures, the filled dots represent the ISM abundances, and the five empty five peaks stars represent our B-type supergiants O/H abundances. As can be seen, the agreement between the results by the N2 indicator and the B-type supergiants is very good, showing only a large departure for the outer parts of the galaxy disk.

Table 6 (see also Fig. 11) summarizes the ISM O/H gradient obtained with the different strong-line method calibrations, as well as the stellar gradient. The latter has been determined both from our analysis of B-type supergiants and from the previous studies on the A-type supergiants by Bresolin et al. (2002a, empty diamonds in Fig. 11) and on the WN11 star analysed by Bresolin et al. (2002b, the four-peak star in the same figure). For this last object, we have assumed that the sum of the C, N and O abundances (by number) does not change during the evolution of the star, being therefore a measurement of the ZAMS global metallicity, which is then translated to a ZAMS oxygen abundance by adopting a solar abundance pattern (which is actually only strickly justified if the derived metallicity is close to solar). We must also point out that oxygen abundances for the A-type supergiants are not measured directly. We have transformed the global metallicity indicator obtained by Bresolin et al. (2002a, see also Przybilla 2002) into oxygen abundance assuming the same relation between the global metallicity and the oxygen abundance as in the Sun. This can be particularly dangerous for A-8, the star with the lowest derived metallicity, as Galactic metal-poor stars show [O/Fe] =+0.4 near [Fe/H] =-1.0 (Asplund & García Pérez 2001; García López et al. 2001; Fulbright & Jonhson 2003). Note also that the derived results depend on the zero-point of the O/H scale (the solar abundance): while Przybilla (2002) reports 8.53 and 8.13 for D-13 and A-8 respectively we found a shift of -0.2 dex due to the change of the solar O/H abundance from the value of Grevesse & Sauval (1998) to the one by Allende Prieto et al. (2001).

It is clear that the Zaritsky et al. (1994) and the Dopita & Evans (1986) calibrations produce steep oxygen gradients, with central values well above the solar abundance. This is in contrast with the other two R_{23} calibrations, which produce a shallower gradient with a central abundance slightly above the solar value. Although the results obtained with Pilyugin's R_{23} calibration well match the stellar oxygen abundances, the calibration by Kobulnicky et al. (1999) also produces results that can be considered in agreement with the stellar ones. Furthermore, the ISM abundances derived by means of the N2 - O/H calibration by Pettini & Pagel (2004) are also in good agreement with the stellar results. Skillman, Côté & Miller (2003) have investigated the ISM abundances in dIrr galaxies of the Sculptor Group, discussing the differences one obtains by applying the R_{23} calibration by Pilyugin (2000) and the one by Kobulnicky et al. (1999) for the low metallicity branch. The results discussed

above for the high metallicity range are in agreement with their findings.

The results obtained from the analysis of B-type supergiants, which are in agreement with the ISM strong method abundances obtained with the R_{23} calibrations by KKP99 and P01, and with the N2 calibration by PP04, indicate that the central parts of NGC 300 are not significantly more metal-rich than the Sun, and that the gradient is shallower that previously thought. Both results are consistent with the recent ones in M 101 by Kennicutt et al. (2003), for which the authors find a shallower gradient and a near-solar metallicity in the inner parts of the galaxy from their analysis of H II regions by the $T_{\rm e}$-method. Moreover, in our work on M 33 (Urbaneja et al. 2004, in prep.) we have found very good agreement between the results from the analysis of intermediate resolution (R $\sim$ 5000) optical spectra of early B-type supergiants and the H II region oxygen abundances derived using a direct method by Vílchez et al. (1988).

4.2. Silicon, Magnesium and metallicity gradients

One of the advantages of the stellar analysis is that we can also obtain the radial gradients of two α-elements, silicon and magnesium, which are not available from H II region optical spectra. The radial gradients for both elements as well as for our global metallicity indicator are summarized in Table 7, and their spatial behaviours are displayed in Fig. 12.

For Mg and Si we find a radial gradient of $-0.064\,(\pm\,0.050)$ dex kpc^{-1} and $-0.068\,(\pm\,0.050)$ dex kpc^{-1} , respectively. Both α-element gradients correlate very well with the oxygen gradient, as well as with each other, which is in agreement with the present understanding of chemical stellar and galactic evolution. The abundances of magnesium and silicon are consistent with a solar metallicity (7.58 and 7.56 dex respectively, from Grevesse & Sauval 1998) for the central regions of NGC 300, as is the case for oxygen. There are no indications, within the uncertainties of the stellar results, of the problem found in our Galaxy by Smartt et al. (1997b), who obtain a flattening of the stellar O abundance in the inner parts of the Milky Way while the other α-element abundances still rise.

4.3. Discussion

Recently, Schild et al. (2003) have completed a survey of Wolf-Rayet stars in the central regions of NGC 300 ($\rho/\rho_0 < 0.5$), obtaining a WC to WN subtype ratio of 0.35. With this ratio and the oxygen value given by Deharveng et al. (1988), Schild et al. conclude from their

Figure 8 that this galaxy deviates somewhat from the relation between the WC/WN ratio and metallicity found in other galaxies of the Local Group (see references in the their paper). With our new determination of the oxygen abundance in the central regions of NGC 300, the Schild et al. (2003) ratio nicely fits the Local Group trend (see Fig. 13), where the data for the Local Group galaxies have been taken from Massey (2003). ISM abundances in the Local Group galaxies have been obtained using both direct methods (through electronic temperatures) and strong line methods. In particular, the regime above 0.5 $Z_{\odot}$ is based mainly on strong-line methods, even for M33 (Vílchez et al. 1988) which probably represents the best case among the LG galaxies. Therefore the quoted ISM O/H abundances could be affected by cautionary considerations similar to those presented in this paper (this is the case, for example, of M 31, see the discussion in Trundle et al. 2002). However, our analysis of early B-type supergiants in M 33 (Urbaneja et al. 2004, in prep.) confirms the location of the three points corresponding to the WC/WN number ratio at different galactocentric distances (labeled in Fig. 13 as M33(o), M33(m) and M33(i), for outer, middle and inner ratios, see Massey 2003 for further details) that define this galaxy, which closely resembles NGC 300 in its structural properties.

Finally, it is interesting to consider the B-type supergiants of NGC 300 within the framework of the Flux-Weighted Gravity–Luminosity Relationship (FGLR). As shown by Kudritzki, Bresolin & Przybilla (2003), a good correlation is found in blue supergiants of type B8 to A4 between the stellar luminosity and the combination of surface gravity and effective temperature $g/T_{eff,4}^4$ (T in units of 10^4 K). For 14 supergiants in NGC 300, a linear fit to the observations showed a dispersion in the bolometric luminosity of only 0.26 magnitudes. In Fig. 14 we show the position in the M_{bol} vs $\log g/T_{eff,4}^4$ diagram occupied by the six B-type supergiants analyzed in the current work (filled circles). The dashed line represents the linear fit determined by Kudritzki, Bresolin & Przybilla (2003) to their sample of blue supergiants in NGC 300 (open star symbols) and other blue supergiants in additional galaxies (open squares, see the last reference for detailed information). The agreement between the new data and the regression line is remarkable, even if we must note that the early B supergiants fill only the high-luminosity end of the diagram. This finding gives additional thrust to the concept behind the FGLR, and suggests that its validity could be extended to earlier spectral types than originally believed. The advantage for the use of the FGLR as an extragalactic stellar distance indicator is obvious, since a larger number of objects could be used among the brightest stars commonly found in spiral galaxies.

5. Conclusions

We have carried out a detailed analysis of B-type supergiants in NGC 300, located beyond the Local Group. We have obtained a chemical abundance pattern which includes the key elements C, N and O, as well as Mg and Si. Our analysis has allowed us to study the degree of chemical evolution for each star. All stars but one show CN contaminated abundances, while O correlates well with Mg and Si, as expected in the case it has not yet been modified by the stellar evolution. The abundance determination has allowed us to trace the α-elements gradients, and compare the oxygen abundance gradient with the one obtained from H II regions. From this comparison, it has been demonstrated that previous determinations overestimated the metallicity gradient and that the central region of the galaxy is not more metal-rich that the Sun. Finally, it has been shown that the analysis of B-type supergiants, even at low resolution, is a powerful tool for extragalactic astrophysics.

We acknowledge the many fruitful discussions and comments by C. Esteban and B. Cedrés. Also, many thanks to G. Meynet and A. Maeder for hepful discussion on the comparison to evolutionary models. This work has been partly supported by the spanish MCyT under project PNAYA 2001-0436. WG and GP acknowledge financial support for this work by the chilean FONDAP Center for Astrophysics 15010003.

REFERENCES

Allende Prieto, C., Lambert, D. L. & Asplund, M. 2001, ApJ, 556, L63

Asplund, M & García Pérez , A. E. 2001, A&A, 372, 610

Bresolin, F., Kudritzki, R.-P., Méndez, R. H., & Przybilla, N. 2001, ApJ, 548, L159

Bresolin, F., Gieren, W., Kudritzki, R.-P., Pietrzyński, G., & Przybilla, N. 2002, ApJ, 567, 277 (a)

Bresolin, F., Kudritzki, R.-P., Najarro, F., Gieren, W. & Pietrzyński, G. 2002, ApJ, 577, L107 (b)

Bresolin, F., Kudritzki, R.-P., Lennon et al. 2002, ApJ, 580, 213 (c)

Bresolin, F., Garnett, D.R., & Kennicutt, R.C. 2004, ApJ, submitted (a)

Bresolin, F., Pietrzyński, G., Gieren, W. & Fouqué, P. 2004, ApJ, 600, 182 (b)

Carollo, C. M. & Lilly, S. J. 2001, ApJ, 548, L153

Castellanos, M., Díaz, A.I., & Terlevich, E. 2002, MNRAS, 329, 315

Cedrés, B. 2003, Ph.D. Thesis, Universidad de La Laguna

Charlot, S. & Longhetti, M. 2001, MNRAS, 323, 887

Christensen, T., Petersen, L. & Gammelgaard, P. 1997, A&A, 322, 41

Deharveng, L., Caplan, J., Lequeux, J., Azzopardi, M., Breysacher, J., Tarenghi, M. & Westerlund, B. 1988, A&AS, 73, 407

Denicoló, G., Terlevich, R., & Terlevich, E. 2002, MNRAS, 330, 69

Díaz, A. I. & Pérez-Montero, E. 2000, MNRAS, 312, 130

D'Odorico, S., Rosa, M. & Wampler, E. J. 1983, A&AS, 53 ,97

Dopita, M. A. & Evans, I. N. 1986, ApJ, 307, 431

Edmunds, M. G. & Pagel, B. E. J. 1984, MNRAS, 211, 507

Evans, C. J., Lennon, D. J., Trundle, C., Heap, S. R. & Lindler, D. J. 2004, ApJ, 607, 451

Freedman, W. L., et al. 2001, ApJ, 553, 47

Fulbright, J. P. & Jonhson, J. A. 2003, ApJ, 595, 1154

García López, R. J. et al. 2001, NewAR, 45, 519

Garnett, D. R., Kennicutt, R.C., & Bresolin, F. 2004, ApJ, in press (astroph/0408319)

Garnett, D. R. 2004, *Element Abundances in Nearby Galaxies*, in the XIII Canary Islands Winter School of Astrophysics on "Cosmochemistry", ed. C. Esteban, R. Garcia López, A. Herreo, & F. Sánchez (Cambridge: Cambridge University Press)

Garnett, D. R., Shields, G. A., Skillman, E. D., Sagan, S. P. & Dufour, R. J. 1997, ApJ, 489, 63

Gehren, T., Kudritzki, R.-P., Butler, K. & Niessen, P. E. 1985, *Abundance Gradients in the Galactic Disk from Young B-Type Stars in Clusters: First Results*, in Proc. ESO Workshop on "Production and Distribution of C, N, O Elements", ed. I. J. Danziger

Gieren, W., Geisler, D., Richtler, T., Pietrzynski, G., & Dirsch, B. 2001, The ESO Messenger, 106, 15

Grevesse, N. & Sauval, A. J. 1998, Space Sci. Rev., 85, 161

Heger, A. & Langer, N. 2000, ApJ, 544, 1016

Herrero, A., Puls, J., & Najarro, F. 2002, A&A, 396, 949

Herrero, A. 2003, in IAU Symp. 212, A Massive Star Odyssey: From Main Sequence to Supernova, ed. K. van der Hucht, A. Herrero & C. Esteban (San Francisco: ASP), 3

Kaufer, A., Venn, K. A., Tolstoy, E., Pinte, C. & Kudritzki, R. P. 2004, AJ, 127, 2723

Kennicutt, R. C. Jr., Bresolin, F. & Garnett, D. R. 2003, ApJ, 591, 801

Kewley, L. J. & Dopita, M. A. 2002, ApJS, 142, 35

Kobulnicky, H. A., Kennicutt, R. C. Jr. & Pizagno, J. L. 1999, ApJ, 514, 544

Kudritzki, R.-P., Lennon, D. J. & Puls, J. 1995, *Quantitative spectroscopy of luminous blue stars in distant galaxies*, in Proc. ESO Workshop "Science with VLT", Eds. J. P. Welsh & I. J. Danziger

Kudritzki, R.-P., Puls, J., Lennon, D. J. et al. 1999, A&A, 350, 970

Kudritzki, R.-P. & Puls, J. 2000, ARA&A, 38, 613

Kudritzki, R.-P. 2002, ApJ, 577, 389

Kudritzki, R.-P., Bresolin, F., & Przybilla, N. 2003, ApJ, 582, L83

Lamers, H. J. G. L. M., Snow, T. P. & Lindholm, D. M. 1995, ApJ, 455, 269

Lilly, S.J., Carollo, C.M., & Stockton, A.N. 2003, ApJ, 597, 730

Maeder, A. & Meynet, G. 2000, ARA&A, 38, 143

Massey, P. 2003, ARA&A, 41, 15

McCarthy, J. K., Lennon, D. J., Venn, K. A., Kudritzki, R. P., Puls, J., & Najarro, F. 1995, ApJ, 455, L135

McCarthy, J. K., Kudritzki, R. P., Lennon, D. J., Venn, K. A., & Puls, J. 1997, ApJ, 482, 757

McErlean, N. D., Lennon, D. J. & Dufton, P. L. 1999, A&A, 349, 553

McGaugh, S. S. 1991, ApJ, 380, 140

Meynet, G. & Maeder, A. 2003, A&A, 404, 975

Meynet, G. & Maeder, A. 2004, A&A, in press

Monteverde, M. I., Herrero, A., Lennon, D. J. & Kudritzki, R. P. 1997, ApJ, 474, L107

Monteverde, M. I., Herrero, A. & Lennon, D. J. 2000, ApJ, 545, 813

Osterbrock, D. E. 1989, Astrophysics of Gaseous Nebulae and Active Galactic Nuclei (Mill Valley: University Science Books)

Pagel, B. E. J. 1997, Nucleosynthesis and Chemical Evolution of Galaxies (Cambridge: Cambridge University Press)

Pagel, B. E. J., Edmunds, M. G., Balckwell, D. E., Chun, M. S. & Smith, G.l. 1979, MNRAS, 189, 95

Pettini, M., & Pagel, B.E.J. 2004, MNRAS, 348, L59

Pietrzyński, G., Gieren, W., Fouqé, P. & Pont, F. 2002, AJ, 123, 789

Pilyugin, L. S. 2000, A&A, 362, 325

Pilyugin, L. S. 2001, A&A, 369, 594

Pilyugin, L. S. 2003, A&A, 399, 1003

Puls, J., Springmann, U. & Lennon, M. 2000, A&AS, 141, 23

Puls, J.. Repolust, T., Hoffmann, T. L., Jokuthy, A. & Venero, R. O. J. 2003, in IAU Symp. 212, A Massive Star Odyssey: From Main Sequence to Supernova, ed. K. van der Hucht, A. Herrero & C. Esteban (San Francisco: ASP), 206

Przybilla, N. 2002, Ph.D. Thesis, University of Munich

Repolust, T., Puls, J. & Herrero, A. 2004, A&A, 415, 349

Santolaya-Rey, E., Puls, J. & Herrero, A. 1997, A&A, 323, 488

Schild, H. Crowther, P. A., Abbott, J. B. & Schmutz, W. 2003, A&A, 397, 859

Skillman, E. D. 1989, ApJ, 347, 883

Skillman, E. D., Côté, J. & Miller, B. W. 2003, AJ, 125, 593

Smartt, S. J. & Rolleston, W. R. J. 1997, ApJ, 481, L47 (a)

Smartt, S. J., Dufton, P. L. & Lennon, D. J. 1997, A&A, 326, 763 (b)

Smartt, S. J., Crowther, P. A., Dufton, P. L. et al. 2001, MNRAS, 325, 257

Smartt, S. J., Lennon, D. J., Kudrityzki, R.-P., Rosales, F., Ryans, R. S. I., & Wright, N. 2002, A&A, 979, 991

Stasińska, G. 2004, *Abundance determinations in HII regions & planetary nebulae*, in the XIII Canary Islands Winter School of Astrophysics on "Cosmochemistry", ed. C. Esteban, R. Garcia López, A. Herreo, & F. Sánchez (Cambridge: Cambridge University Press)

Steidel, C.C., Shapley, A.E., Pettini, M., Adelberger, K.L., Erb, D.K., Reddy, N.A., & Hunt, M.P. 2004, ApJ, 604, 534

Storchi-Bergmann, T., Calzetti & D., Kinney, A. L. 1994, ApJ, 429, 572

Trundle, C., Dufton, P. L., Lennon, D. J., Smartt, S. J. & Urbaneja, M. A. 2002, A&A, 395, 519

Unsöld, A. 1955, Physik der Sternatmosperen (2nd ed.; Berlin: Springer-Verlag)

Urbaneja, M. A., Herrero, A., Kudritzki, R. P. et al. 2002, A&A, 386, 1019

Urbaneja, M. A., Herrero, A., Bresolin, F., Kudritzki, R.-P., Gieren, W. & Puls, J. 2003, ApJ, 584, L73

Urbaneja, M. A. 2004, Ph.D. Thesis, University of La Laguna

Venn, K. A., McCarthy, J. K., Lennon, D. J., Przybilla, N., Kudritzki, R. P. & Lemke, M. 2000, ApJ, 541, 610

Venn, K. A., Tolstoy, E. Kaufer, A. et al. 2003, AJ, 126, 1326

Vila-Costas, M. B. & Edmunds, M. G. 1992, MNRAS, 259, 121

Vílchez, J. M., Pagel, B. E. J., Díaz, A. I., Terlevich, E. & Edmunds, M. G. 1988, MNRAS, 235, 633

Vink, J., de Koter, A. & Lamers, H. J. G. L. M. 2000, A&A, 362, 295

Vink, J., de Koter, A. & Lamers, H. J. G. L. M. 2001, A&A, 369, 574

Webster, B. L. & Smith, M. G. 1983, MNRAS, 204, 743

Woosley, S. E., Heger, A. & Weaver, T. A. 2002, Reviews of Modern Physics, 74, 1015

Zaritsky, D., Kennicutt, R. C. Jr. & Huchra, J. P. 1994, ApJ, 420, 87

Table 1. Best-fit model parameters.

	A-9	B-12	B-13	B-15	C-14	D-8
RA (J2000)[a]	0 55 39.262	0 54 56.083	0 54 56.754	0 55 03.464	0 54 26.881	0 54 31.235
Dec (J2000)[a]	-37 41 18.23	-37 41 04.02	-37 41 33.79	-37 42 26.18	-37 37 34.41	-37 41 55.96
$\rho\,/\,\rho_0$[b]	0.97	0.05	0.09	0.26	0.66	0.52
SpT[a]	B1	B0.5	B3	B1.5-B2	B1	B1.5
Teff (10^3 K)	21.0±1.0	24.0±1.0	17.0±1.0	19.0±1.0	22.0±1.0	19.0±1.0
log g (cgs)	2.50±0.15	2.60±0.15	2.00±0.15	2.30±0.20	2.65±0.15	2.30±0.15
v_∞ (km s^{-1})	*1200.*	*1500.*	*500.*	*600.*	*1200.*	*600.*
$\dot{M}$ (10^{-6} $M_\odot\,yr^{-1}$)	0.47±0.12	3.44±0.50	0.92±0.07	2.07±0.60[c]	0.46±0.14	0.36±0.10
R/R$_\odot$	31.6±1.0	46.2±1.5	80.3±2.0	48.3±1.5	30.4±1.0	49.5±2.0
β	2.00±0.25	1.25±0.25	2.00±0.25	*2.00*	2.00±0.25	2.00±0.25
Y_{He}	0.10	0.10	0.15	0.10	0.10	0.10
v_{turb} (km s^{-1})	15.	20.	12.	15.	17.	15.
ϵ_C	7.60	8.00	8.00	8.10	7.70	7.50
ϵ_N	8.00	7.50	8.25	8.25	7.75	8.10
ϵ_O	8.30	8.65	8.45	8.55	8.35	8.25
ϵ_{Mg}	7.20	7.50	8.10[d]	7.40	7.05	7.25
ϵ_{Si}	7.10	7.45	7.35	7.45	7.05	7.25
Z ($Z_\odot$)	0.30	1.00	0.60	0.80	0.50	0.40
$[M\,/\,H]$ (dex)	-0.50	0.00	-0.20	-0.10	-0.30	-0.40
Log (L/L$_\odot$) (cgs)	5.47±0.11	5.96±0.10	5.78±0.11	5.47±0.12	5.50±0.11	5.49±0.13
M^{spec}/M$_\odot$	12.0±5.0	31.0±13.0	26.0±10.0	17.0±7.0	15.0±6.0	18.0±7.7
Log D$_{mod}$ (cgs)	28.30 ± 0.16	29.34 ± 0.16	28.42 ± 0.17	28.66 ± 0.22[c]	28.28 ± 0.14	27.98 ± 0.19

[a]From Bresolin et al. (2002a).

[b]Galactocentric distance, in units of the isophotal radius $\rho_0 = 9.75$ arcmin. Coordinates for the center of NGC 300 AR 00 54 53.5 Dec -37 41 03.8 (J2000)

[c]Upper limit, see text for comments.

[d]See text for comments.

Note. — The metal abundances are expressed as $\epsilon_A = 12 + log(A/H)$, while $[M/H] = log(M/H)_* - log(M/H)_\odot$. Adopted quantities are quoted in italics, without uncertainties.

Table 2. Observed and synthetic magnitudes.

	Observed		Synthetic				
ID	V	$B-V$	M_V	M_B-M_V	BC	$Mbol$	$E(B-V)$
A-9	20.24	-0.13	-6.38	-0.16	-2.55	-8.93	0.03
B-12	19.28	-0.11	-7.44	-0.17	-2.72	-10.15	0.06
B-13	18.64	-0.08	-7.98	-0.11	-1.74	-9.72	0.03
B-15	19.71	-0.04	-7.10	-0.14	-1.80	-8.90	0.10
C-14	20.28	-0.14	-6.37	-0.18	-2.63	-9.00	0.04
D-8	19.50	-0.09	-7.19	-0.14	-1.79	-8.98	0.05

Note. — We adopted a distance modulus $\mu = 26.53 \pm 0.07$ (Freedman et al. 2001), and $R_v = 3.1$ for estimating the extinction from derived reddenings.

Table 3. Abundance uncertainties obtained from the grid of models. The influence of the uncertainties in each fundamental parameter is considered. The global abundance uncertainty for each element is obtained as the square root of the sum of the squares of these uncertainties, assuming them to be independent.

			Model 24000 / 2.60				
Element	Line	Δ log g $\pm$ 0.15 dex	ΔT_{eff} $\pm$ 1000 K	Δ v$_{\rm turb}$ $-$ 5 km/s	Δ He $+$ 0.2 dex	Δ Z $-$ 0.2 dex	Δ log Q $\pm$ 0.2 dex
601	λ4267	0.11	0.18	0.10	0.02	0.01	0.01
			σ(C) 0.23 dex				
701	λ3995	0.08	0.18	0.07	0.02	0.02	0.03
701	λ5025	0.03	0.17	0.06	0.05	0.06	0.06
701	λ5045	0.02	0.16	0.06	0.05	0.04	0.05
			σ(N) 0.21 dex				
801	λ4069	0.02	0.07	0.06	0.01	0.00	0.00
801	λ4072	0.01	0.07	0.11	0.01	0.00	0.00
801	λ4076	0.01	0.06	0.13	0.01	0.01	0.00
801	λ4317	0.03	0.07	0.07	0.04	0.02	0.03
801	λ4319	0.03	0.06	0.07	0.03	0.01	0.02
801	λ4414	0.04	0.04	0.10	0.02	0.02	0.00
801	λ4416	0.03	0.06	0.08	0.03	0.01	0.01
			σ(O) 0.14 dex				
1201	λ4481	0.09	0.18	0.07	0.01	0.02	0.02
			σ(Mg) 0.21 dex				

Note. — The element identification is codified as 100$\times$ atomic number plus the ionization stage; for example: 701 corresponds to singly ionized nitrogen.

Table 4. Abundance uncertainties estimation from the grid of models (cont.).

Element	Line	Δ log g ± 0.15 dex	Δ T_{eff} ± 1000 K	Δ v_{turb} − 5 km/s	Δ He + 0.2 dex	Δ Z − 0.2 dex	Δ log Q ± 0.2 dex
			Model 21000 2.50				
601	λ4267	0.09	0.13	0.15	0.01	0.00	0.02
			σ(C) 0.22 dex				
701	λ3995	0.10	0.14	0.10	0.02	0.01	0.02
701	λ5025	0.02	0.16	0.06	0.07	0.06	0.06
701	λ5045	0.00	0.15	0.07	0.05	0.03	0.04
			σ(N) 0.20 dex				
801	λ4069	0.20	0.07	0.08	0.03	0.01	0.01
801	λ4072	0.21	0.08	0.09	0.03	0.01	0.01
801	λ4076	0.20	0.09	0.09	0.03	0.01	0.01
801	λ4317	0.20	0.05	0.09	0.06	0.03	0.02
801	λ4319	0.20	0.05	0.09	0.05	0.02	0.01
801	λ4414	0.20	0.10	0.09	0.04	0.01	0.00
801	λ4416	0.21	0.10	0.09	0.05	0.01	0.01
			σ(O) 0.25 dex				
1201	λ4481	0.09	0.14	0.08	0.01	0.01	0.02
			σ(Mg) 0.19 dex				

Table 5. Relative abundances and abundance ratios (by mass).

ID	Z $Z_\odot$	CNO $CNO_\odot$	[Si/O] dex	N/C	N/O	ρ / ρ_0	ρ arcsec
A-9	0.30	0.48	-0.11 ± 0.28	2.93 ± 1.90	0.44 ± 0.29	0.97	568.
B-12	1.00	0.71	-0.11 ± 0.28	0.37 ± 0.24	0.06 ± 0.04	0.05	31.
B-13	0.60	0.65	-0.01 ± 0.28	2.07 ± 1.35	0.55 ± 0.36	0.09	54.
B-15	0.80	0.77	-0.01 ± 0.28	1.65 ± 1.07	0.44 ± 0.29	0.26	151.
C-14	0.50	0.40	-0.21 ± 0.43	1.30 ± 1.28	0.22 ± 0.21	0.66	385.
D-8	0.40	0.55	0.09 ± 0.27	4.64 ± 3.02	0.62 ± 0.40	0.52	305.

Table 6. Oxygen radial abundance gradient in NGC 300

	Central abundance dex	gradient ρ / ρ_0	gradient dex kpc^{-1}
Dopita & Evans (1986) [a]	8.95 ± 0.04	-0.63 ± 0.10	-0.109 ± 0.017
Zaritsky et al. (1994)	8.98 ± 0.04	-0.54 ± 0.09	-0.094 ± 0.016
Kobulnicky et al. (1999)	8.75 ± 0.04	-0.27 ± 0.09	-0.047 ± 0.016
Pilyugin (2001)	8.52 ± 0.06	-0.28 ± 0.12	-0.049 ± 0.021
Pettini & Pagel (2004)[b]	8.50 ± 0.04	-0.36 ± 0.08	-0.062 ± 0.014
B-type supergiants (this work)	8.58 ± 0.13	-0.32 ± 0.26	-0.055 ± 0.045
B-type supergiants + A-type supergiants[c] + WN11[d]	8.63 ± 0.13	-0.41 ± 0.21	-0.071 ± 0.038

[a]Results taken from Deharveng et al. (1988), after the correction for the distance used in this paper.

[b]Based on the N2 indicator rather than on the R_{23} index.

[c]Abundance results from Bresolin et al. (2002a)

[d]Abundance results from Bresolin et al. (2002b); we have assume a solar-like metallicity pattern for tranforming the actual C+N+O abundance into the original O abundance.

Table 7. Magnesium, silicon and metallicity radial abundance gradients in NGC 300

	Central abundance	gradient ρ / ρ_0	gradient
$\log(Mg/H) + 12$	7.48 ± 0.17 (dex)	-0.37 ± 0.29	-0.064 ± 0.050 (dex kpc^{-1})
$\log(Si/H) + 12$	7.46 ± 0.16 (dex)	-0.39 ± 0.26	-0.068 ± 0.045 (dex kpc^{-1})
Z	0.80 ± 0.22 ($Z_\odot$)	-0.39 ± 0.32	-0.068 ± 0.056 ($Z_\odot$ kpc^{-1})

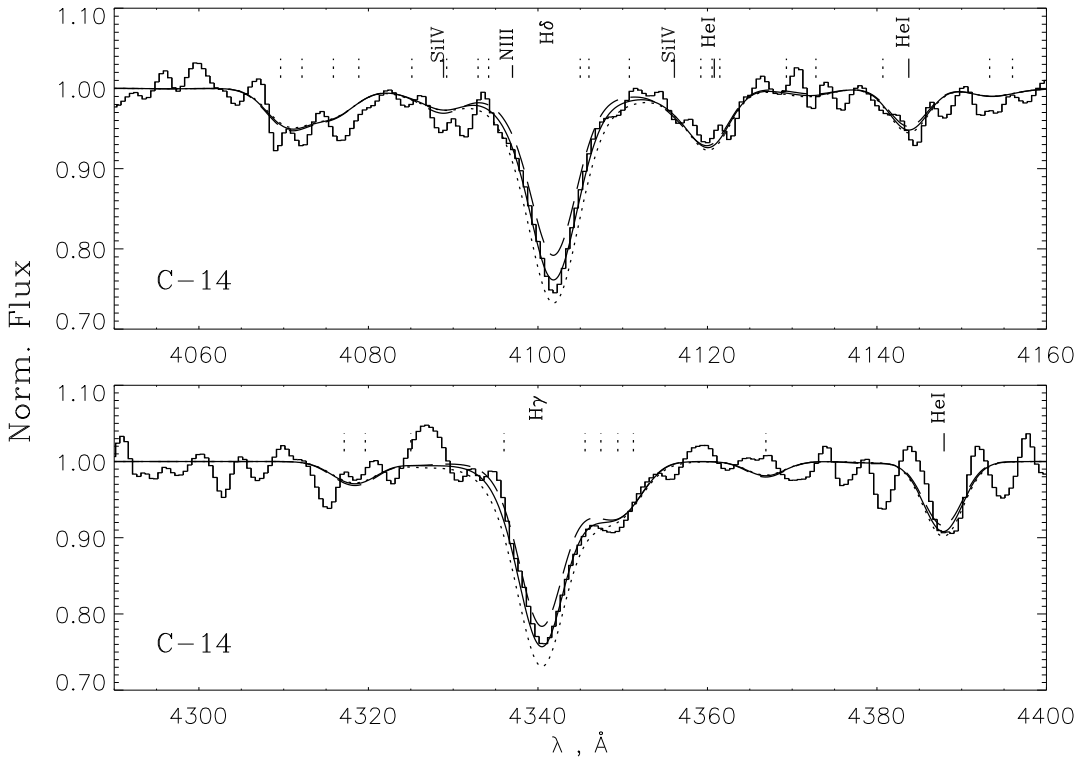

Fig. 1.— Surface gravity uncertainty. The observed Hδ (top panel) and Hγ (lower panel) profiles of the star C-14 are compared with three synthetic models considering three different surface gravities: a model for the final surface gravity derived (solid line) and two other models with surface gravity modified by $\pm\,0.15$ dex (dotted and dashed lines respectively). An identification of some prominent espectral features is also provided. As in the next figure, lines without element identification correspond to singly ionized oxygen lines.

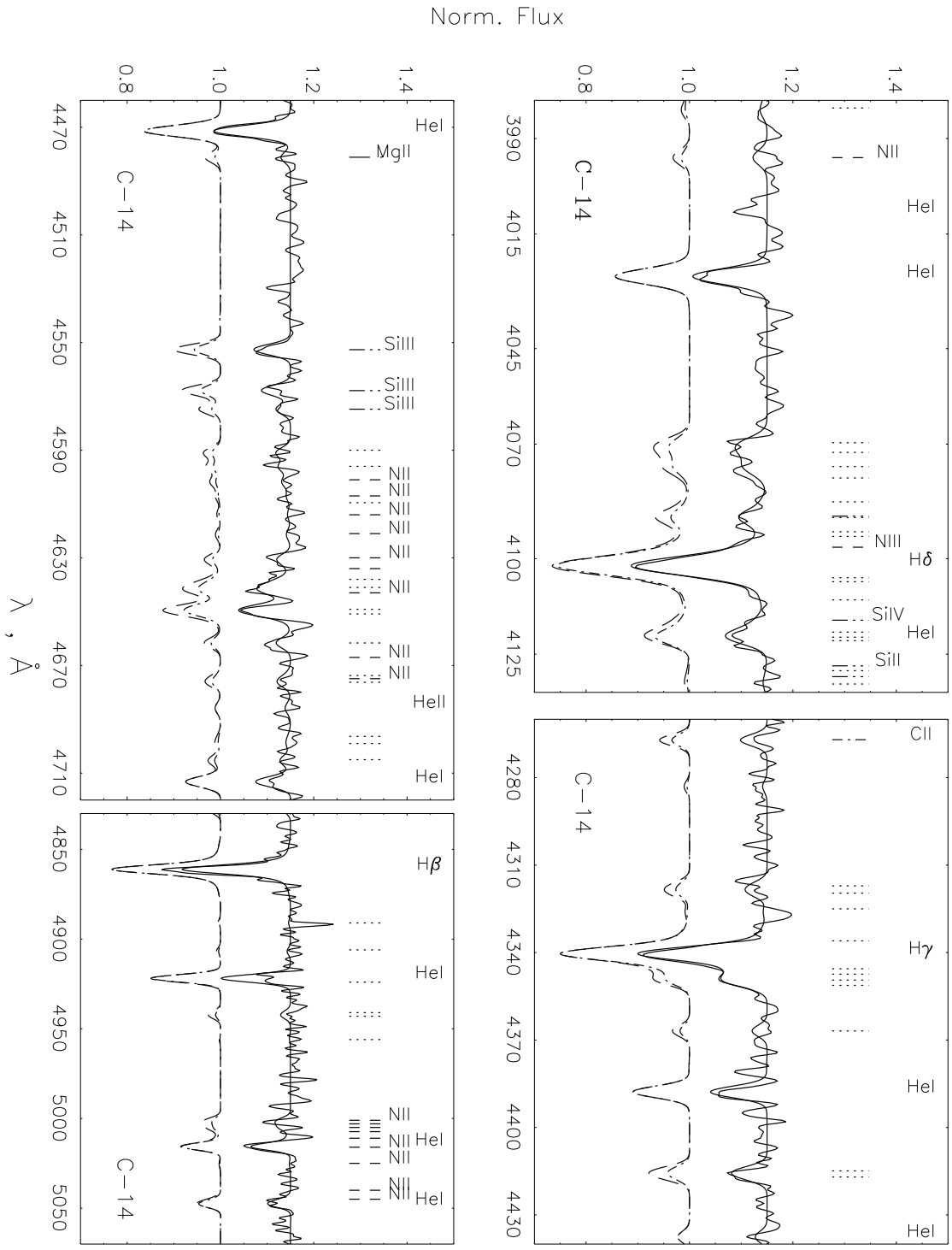

Fig. 2.— Final fit for C-14 in NGC 300. Models with abundances differing by ± 0.3 dex are displayed below the best fit model. The spectra have been arbitrarily shifted in ordinate for the sake of clarity. Lines without element identification correspond to singly ionized oxygen lines.

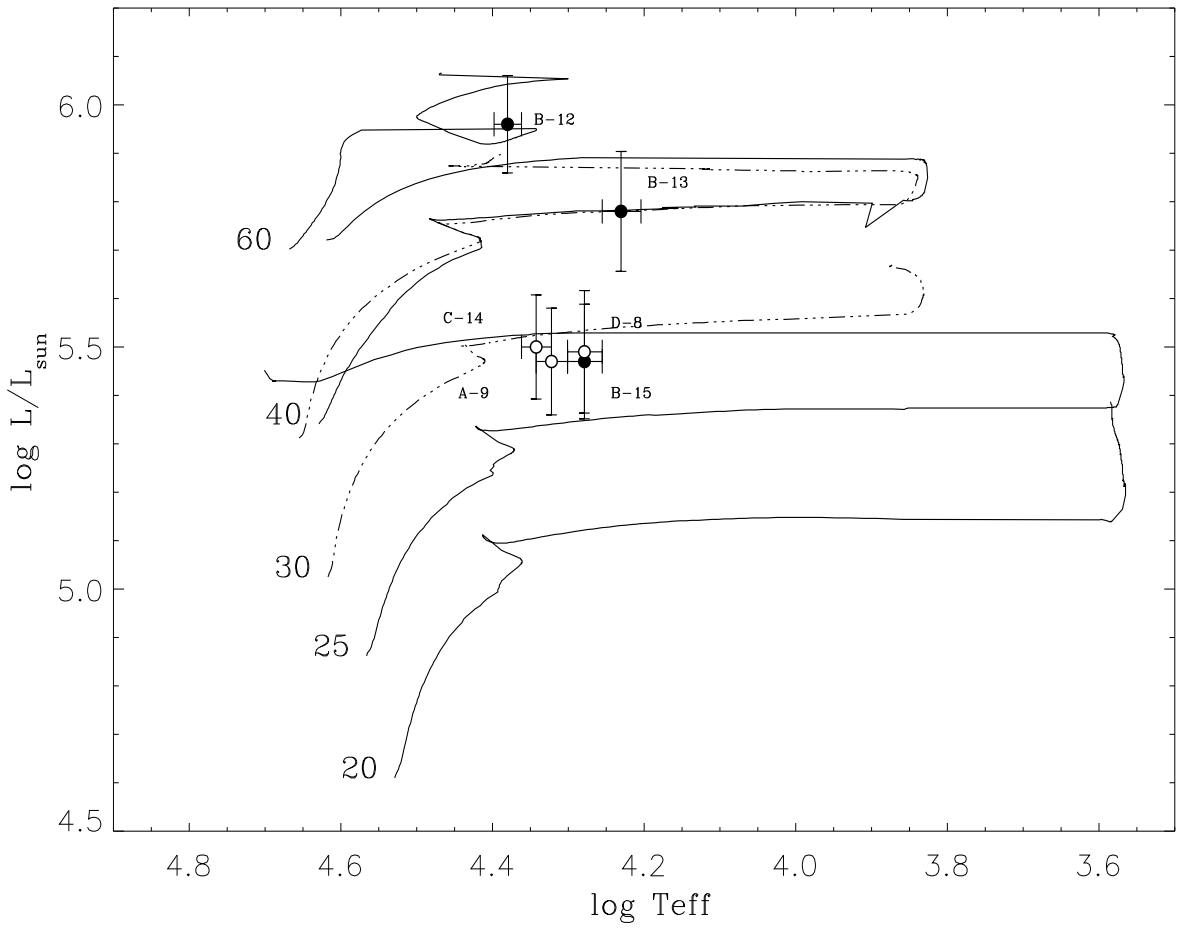

Fig. 3.— Location of the NGC 300 B-type supergiants in the H-R diagram. The theoretical stellar tracks including rotation, for an initial equatorial rotational velocity of 300 km s^{-1}, for $Z_\odot$ (thick solid line) and $1/5\,Z_\odot$ (thin solid line) are taken from Meynet & Maeder (2003) and Meynet & Maeder (2004) respectively. Tracks are labeled with the initial stellar mass. Stars with metallicity above $0.51\,Z_\odot$ are displayed by filled dots while stars below this metallicity are represented by empty dots.

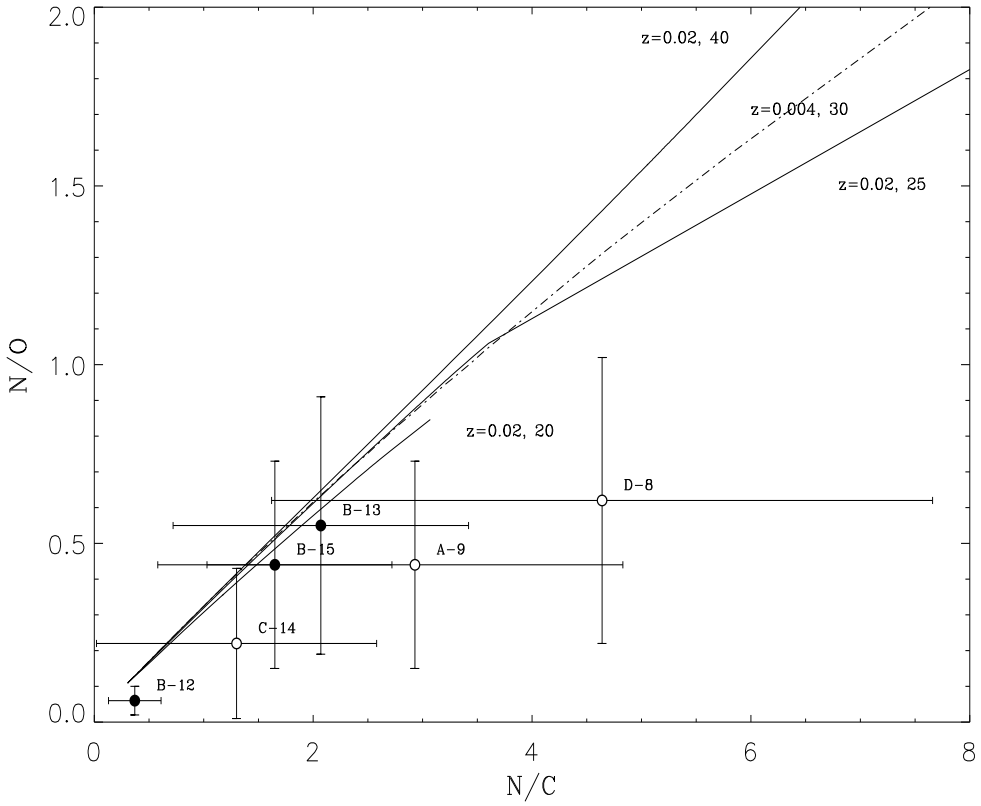

Fig. 4.— Degree of chemical evolution of individual stars (I): the behaviour of the N/O ratio vs N/C ratio. The solid lines correspond to ZAMS solar metallicity models of 40, 25 and 20 $M_\odot$ with an initial equatorial rotation of 300 km s^{-1}, while the dashed line stands for a ZAMS 1/5 $Z_\odot$ model of 30 $M_\odot$ again with initial rotation of 300 km s^{-1}. The NGC 300 stars have been splitted into two groups: the ones with $Z/Z_\odot > 0.51$ (filled dots) and the ones with $Z/Z_\odot < 0.51$ (empty dots). See text for a discussion.

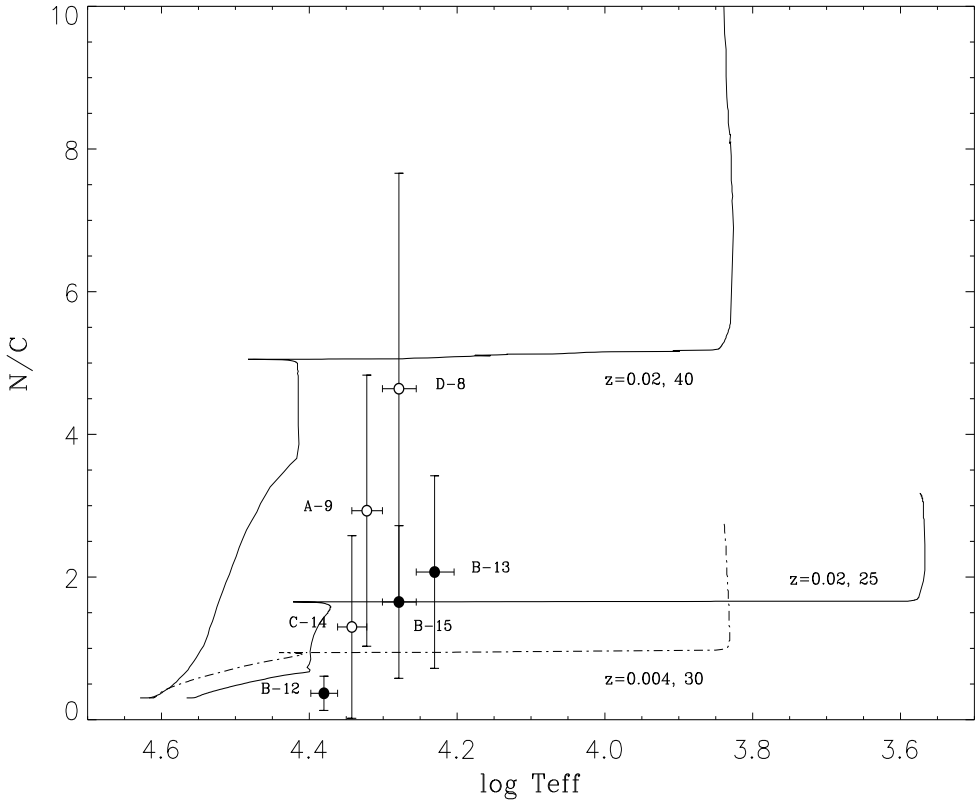

Fig. 5.— Degree of chemical evolution of individual stars (II): the behaviour of the N/C ratio vs Teff. Solid lines correspond to two ZAMS solar metallicity models of 40 and 25 $M_\odot$ with an initial equatorial rotation of 300 km s^{-1}, while the dashed line stands for a ZAMS 1/5 $Z_\odot$ model of 30 $M_\odot$ again with initial rotation of 300 km s^{-1}. As in the previous figure, the NGC 300 stars are shown by filled dots for $Z/Z_\odot > 0.51$ and by empty dots for $Z/Z_\odot < 0.51$. See text for a discussion.

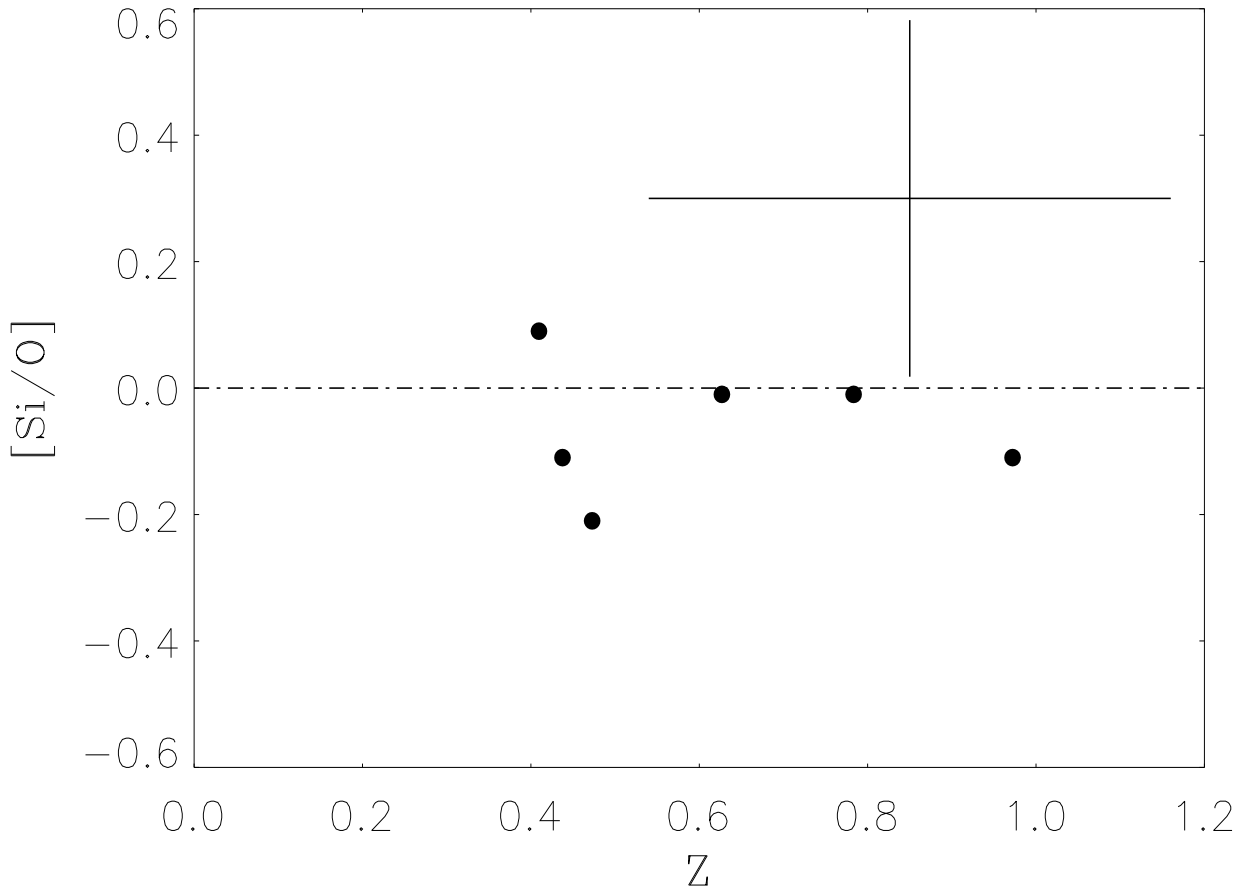

Fig. 6.— Degree of chemical evolution of individual stars (III): the derived Si/O ratio relative to the Sun ratio. A typical error bar is displayed in the upper-right corner. See text for a discussion.

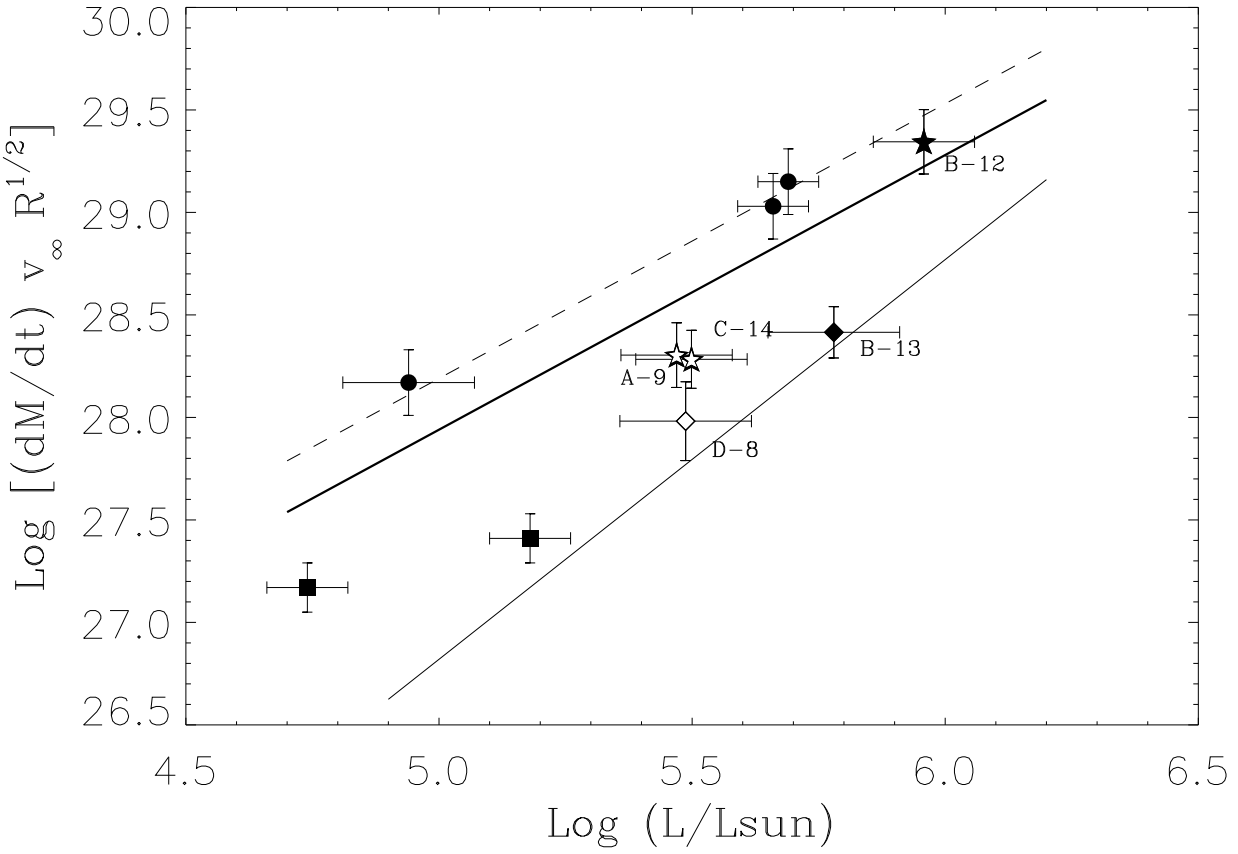

Fig. 7.— Wind Momentum–Luminosity Relationship. Derived modified wind momenta of NGC 300 B-type supergiants are compared to the Galactic results by Kudritzki et al. (1999, solid lines). Filled symbols stand for solar metallicity stars and open symbols represent sub-solar metallicity objects. Circles and stars denote early B-types (B0-B1) while squares and diamonds are used for mid B-types (B1.5 and later types). The Galactic results are taken from new analyses by of means blanketed unified models of some of the Kudritzki et al. (1999) stars by Urbaneja (2004). The dashed line is the original Kudritzki et al. (1999) fit for early types shifted by 0.25 dex. The labels identify the NGC 300 B-type supergiants. See text for an explanation.

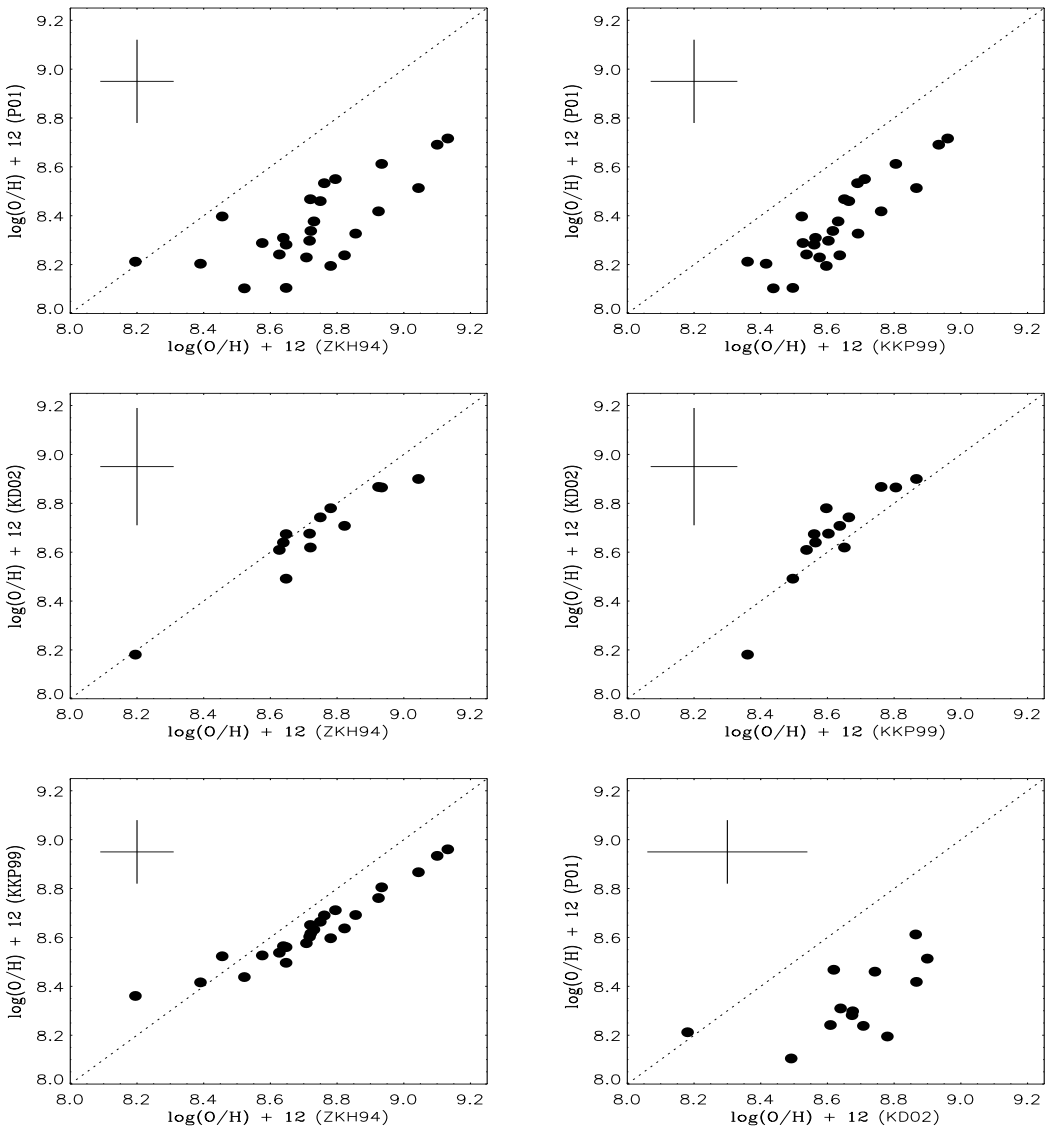

Fig. 8.— NGC 300 ISM oxygen abundances. Comparison between several statistical methods. Each axis is labeled with an identifier of the R_{23} calibration: *ZKH94* for Zaritsky et al. (1994), *KKP99* for Kobulnicky et al. (1999), *P01* for Pilyugin (2001) and *KD02* for the optimal abundance indicator of Kewley & Dopita (2002). Typical error bars are displayed in each plot.

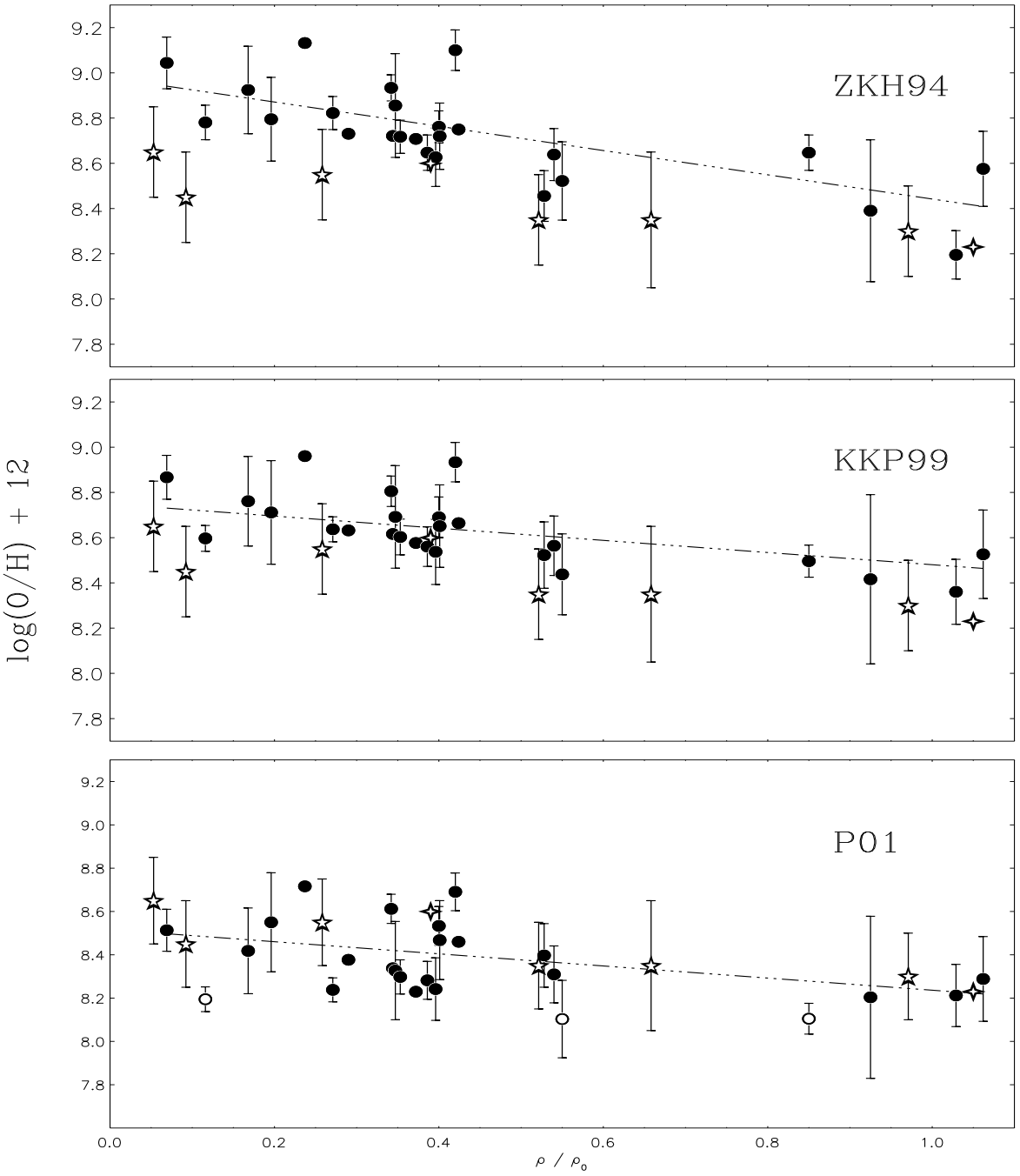

Fig. 9.— The oxygen abundance gradient, comparison between three R_{23} calibrations and the O abundances from B-type supergiants. Each panel is labeled with an identifier of the R_{23} calibration used. Dots are the H II regions results while five-peaks stars are the results obtained from the analysis of B-type supergiants. Empty dots in the P01 panel identify the H II beyond the limits of applicability of this R_{23} - O/H calibration (see text). Weighted least-squares fits to H II oxygen abundances are also shown. Both four-peak empty stars denote the O/H results obtained for two H II regions with T_e measurement (see text for further details).

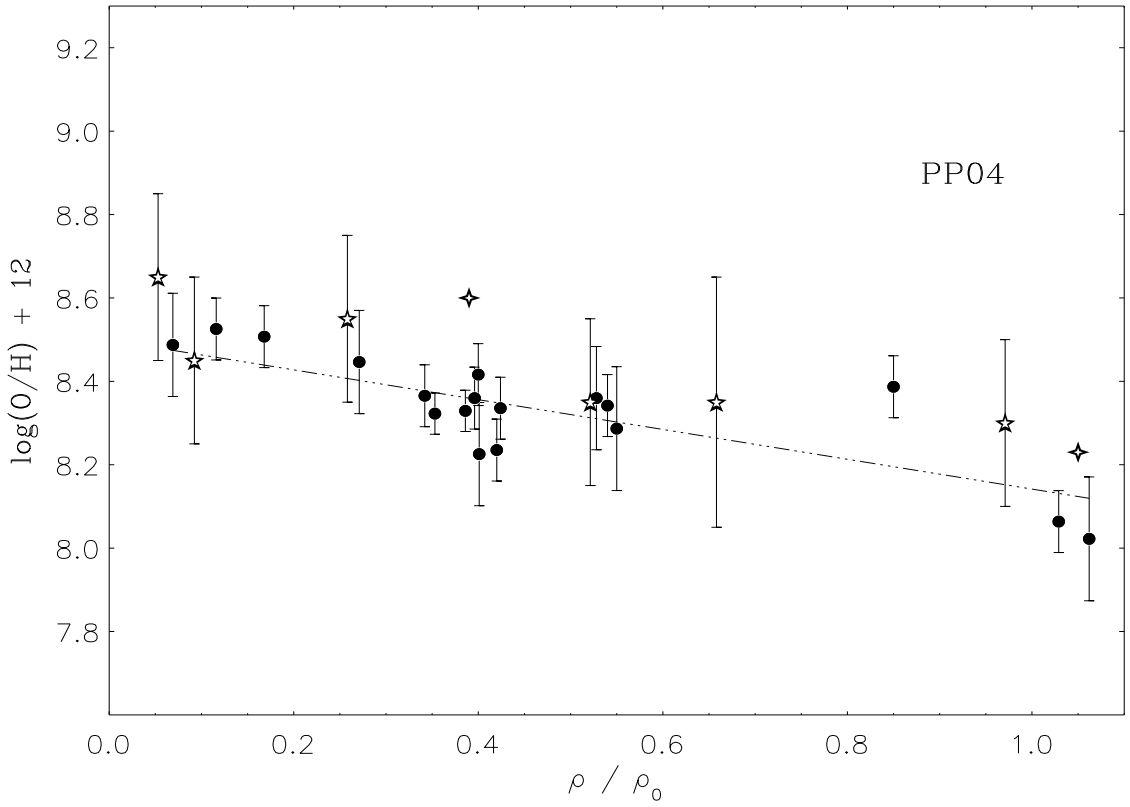

Fig. 10.— Comparison between ISM O/H abundances derived by means of the N2 indicator by Pettini & Pagel (2004) and stellar O/H abundances. As in the previous figure, dots identify the H II O/H regions results while the empty five-peaks stars stand for B-type supergiants abundances. A weighted least-squares fit to H II oxygen abundances is also shown. Both four-peak empty stars denote the O/H results obtained for two H II regions with T_e measurement.

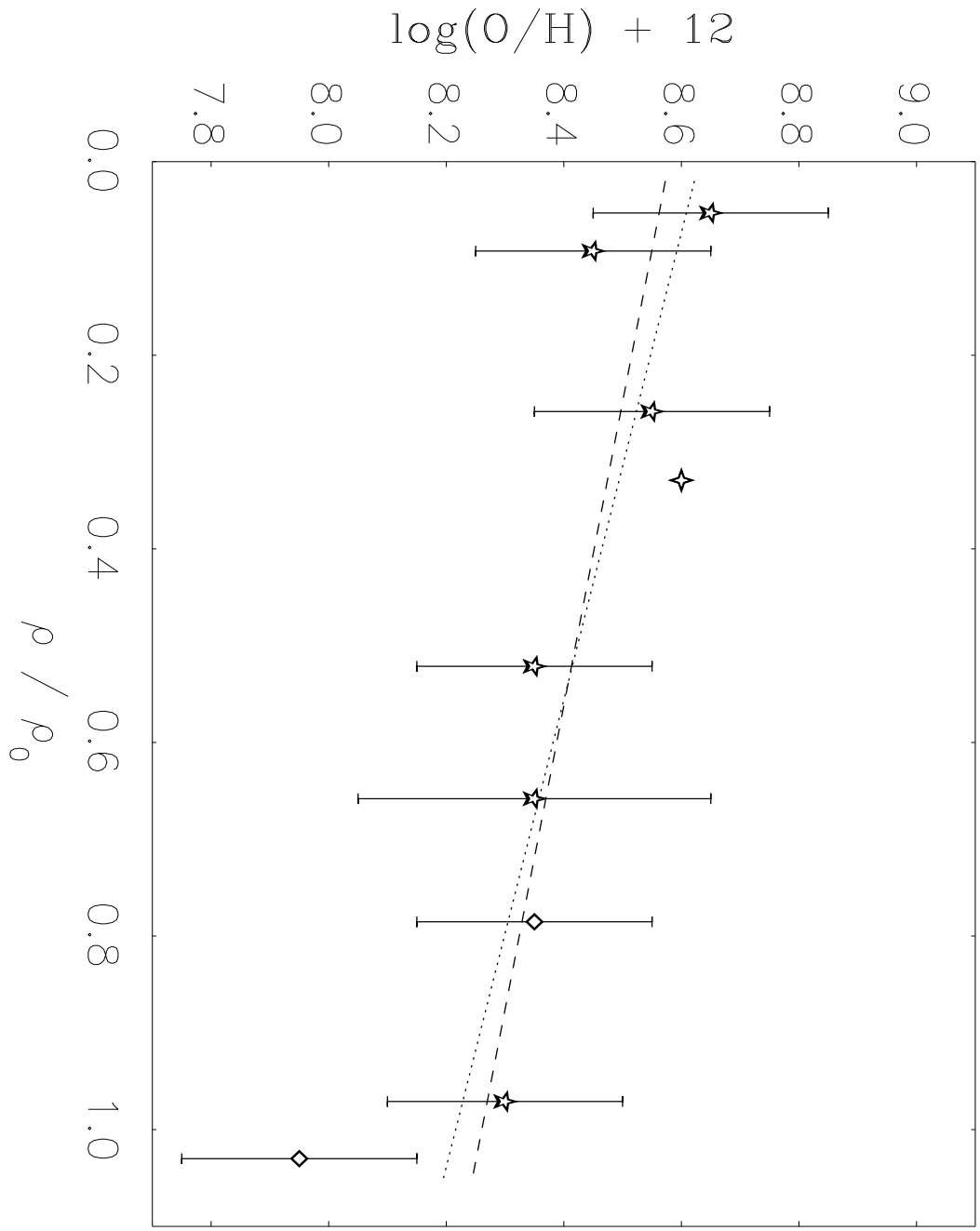

Fig. 11.— Oxygen abundance gradient obtained from the combination of different stellar sources. The two empty diamonds denote the two A-type supergiants presented in Bresolin et al. (2002a), while the four-peak star identifies the WN11 star analysed in Bresolin et al. (2002b). Five-peak stars correspond to the B-type supergiants analysed here. Weighted least-squares fits are overplotted: to the B-type supergiants results (dashed line) and considering all stellar analyses (dotted line). The reader is referred to the text for a clarification about the abundances of both A-type supergiants and of the emission line star.

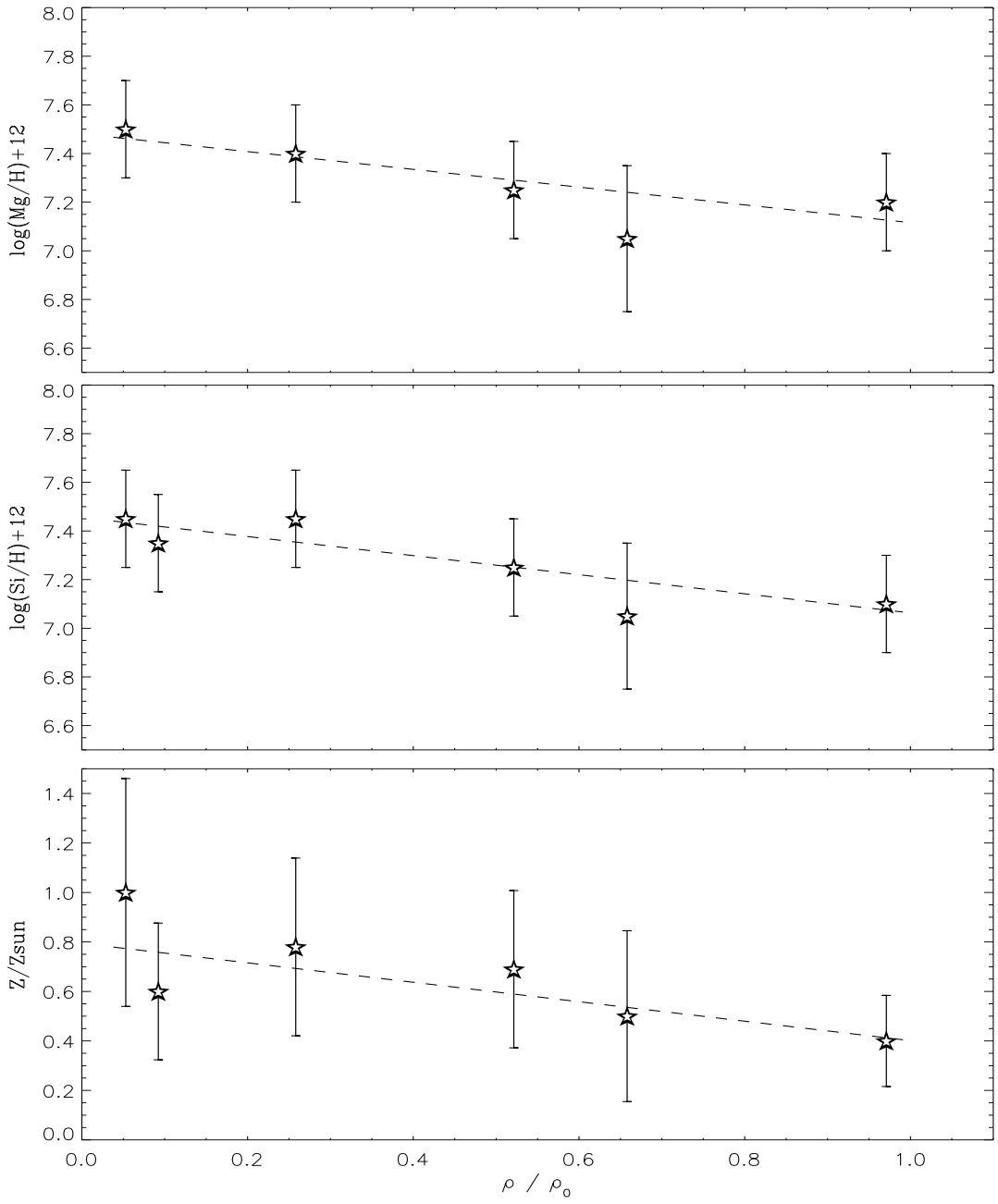

Fig. 12.— Metallicity gradient in NGC 300: spatial behaviour of derived stellar abundances of Mg (top) and Si (center). Both α-elements nicely follow the behaviour found for stellar O/H abundances. The bottom panel displays the spatial trend of our global metallicity indicator, based on O, Mg and Si abundances (note that unlike the two other panels, the y-axis is in a linear scale in this case). Weighted least-squares fits are overplotted as dashed lines.

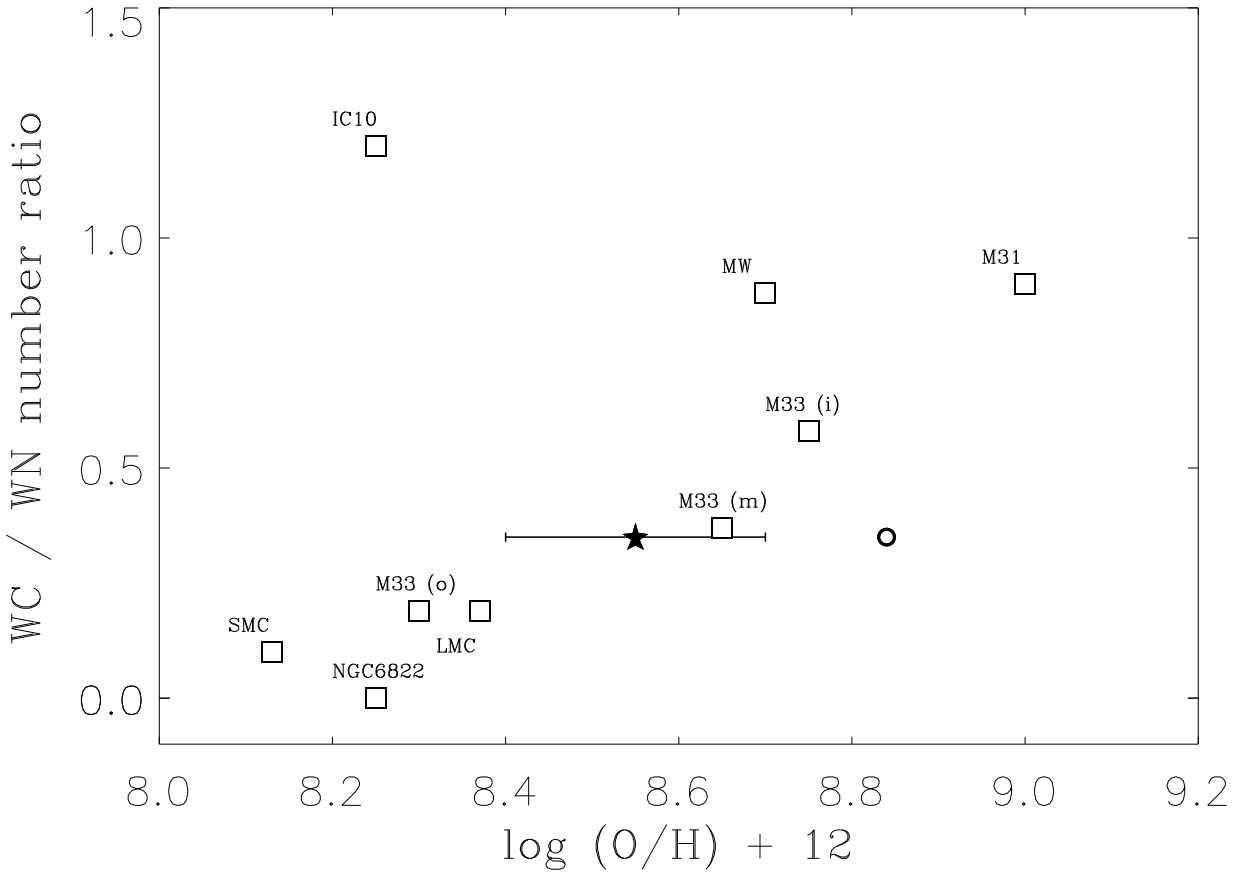

Fig. 13.— Number ratio of WC to WN stars versus ISM oxygen abundances in nearby galaxies. Squares stand for Local Group galaxies (Massey 2003). The Local Group galaxy M 33 is represented by three points, corresponding to the inner, intermediate and outer parts of the galaxy. The empty circle identifies the result for NGC 300 by Schild et al. (2003), who used the abundance value from Deharveng et al. (1988), while the filled star marks the location using our oxygen abundance value. The WC/WN number ratio in NGC 300 has been taken from Schild et al. (2003).

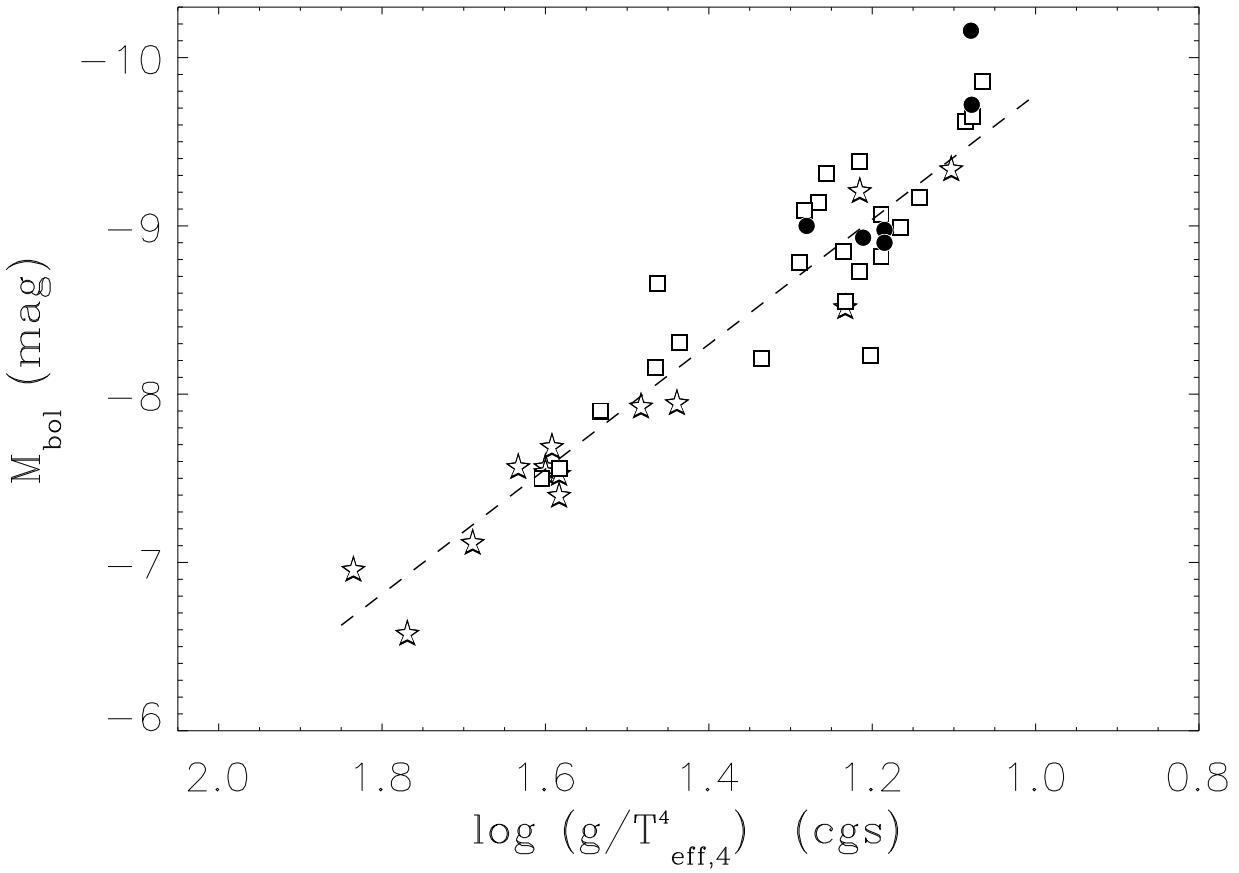

Fig. 14.— Flux-Weighted Gravity–Luminosity Relationship of NGC 300 stars. Early B-type supergiants analysed in the present work (solid cirles) are compared with the FGLR derived by Kudritzki et al. (2003) for AB supergiants in NGC 300 (open star symbols) and other galaxies (open squares). The dashed line represents the linear fit determined by Kudritzki et al. (2003). Teff is used in units of 10^4 K.